Journal of Molecular Structure 1269 (2022) 133793

Contents lists available at ScienceDirect

Journal of Molecular Structure

journal homepage: www.elsevier.com/locate/molstr

Spectral characterization, solvation effects on topological aspects, and biological attributes of Fmoc-L-glutamic acid 5–tert–butyl ester: An effective reagent in anticancer evaluations

M. Thirunavukkarasu[a,b], G. Balaji[b], P. Prabakaran[c], Shaik Jaheer Basha[d], Ahmad Irfan[e], S Saleem Javed[f], S. Muthu[g,*]

[a] Department of Physics, Indo-American College, Cheyyar, Tamil Nadu 604 407, India
[b] Department of Physics, Thiru A Govindasamy Govt. Arts College, (Affiliated to Thiruvalluvar University, Vellore), Tindivanam, Tamil Nadu 604 001, India
[c] Department of Physics, Loyola College, Chennai, Tamil Nadu 600 034, India
[d] Department of Humanities and Sciences (PHYSICS), Annamacharya Institute of Technology and sciences, Kadapa, Andhra Pradesh 516 003, India
[e] Department of Chemistry, College of Science, King Khalid University, P.O. Box 9004, Abha 61413, Saudi Arabia
[f] Department of Chemistry, Institute of H. Science, Khandari, Dr. Bhimrao Ambedkar University, Agra, Uttar Pradesh 282002, India
[g] Department of Physics, Arignar Anna Government Arts College, Cheyyar, Tamil Nadu 604 407, India

ARTICLE INFO

Article history:
Received 24 June 2022
Revised 17 July 2022
Accepted 23 July 2022
Available online 24 July 2022

Keywords:
DFT
Solute-solvent interactions
Vibrational study
NCI-analysis
Molecular docking

ABSTRACT

In this study, the solvation effects, structural characterization, and biological properties of the Fmoc-L-glutamic acid 5-tert-butyl ester (Fmoc-L-Glu(OtBu)) were described with experimental (UV–Vis, FT-IR, and FT-Raman,) and DFT techniques. The topological analysis of the compound was done in order to ensure that self-assembled forces (weak non-bonded contacts) existed between the chemical functionalities (carbonyl, amine, carboxylic acid, & hydroxyl) in the solution phases. The spectral techniques were utilized to assess the compound structure as well as the relationship between potential energy distribution and structural properties. The chemical reactivity has been discussed in terms of Molecular electrostatic potential, FMOs, and Fukui function analyses. Also, the stability and optical properties of the chemical were computationally obtained by NBO and NLO studies. The highest electron transferability of molecular orbitals was examined through UltraViolet-Visible absorptions spectra of Fmoc-L-Glu(OtBu). The effects of polar and non-polar solvents on the title molecule were also detailed using the solute-solvent interaction parameters. The chemical's biological functions were investigated further via molecular docking with cancer cell proteins.

© 2022 Elsevier B.V. All rights reserved.

1. Introduction

The Fmoc-L-glutamic acid 5-tert-butyl ester (Fmoc-L-Glu(OtBu)) is a Fmoc derivative with an N-substituted tert–butyl ester molecule. Fmoc group molecules were reported to have a stable structure, were widely used reagents for a variety of chemical formations, and are important intermediates in the synthesis of pharmaceuticals due to their ability to protect amine groups [1]. The title chemical Fmoc-L-Glu(OtBu), also reacted effectively with a wide range of organic compounds in drug delivery systems for various diseases, including Alzheimer's [2], tuberculosis (TB) [3], cancer [4–9], viral and bacterial [10], inflammatory and was most commonly seen in anti-cancer drug delivery [11–16]. Furthermore, the title molecule and its derivatives have the potential to self-assemble into nano and microscale structures spontaneously [17]. These Fmoc materials are more significant in bio-chemicals and pharmaceuticals because of their low molecular weight, good stability, high aromatic content, low toxicity, minimal side effect, and amine group protecting properties. Also, the self-assembled Fmoc variants could be used in a range of applications such as supramolecular electronics, drug delivery vectors, photonics, and healing agents in regenerative drugs, cell culture, tissue engineering, and other areas of bionanotechnology [18,19]. Many studies have lately detailed the self-assemble property of Fmoc-L-Glu(OtBu) and its derivatives. To recognize such qualities in Fmoc derivatives, a full understanding of structural and electronic aspects is required. As a result of these requirements, many cryptographic investigations of the XRD structure have been reported in various publications. Fmoc derivatives and structurally related title molecules have also been

* Corresponding author.
E-mail address: mutgee@gmail.com (S. Muthu).

https://doi.org/10.1016/j.molstruc.2022.133793
0022-2860/© 2022 Elsevier B.V. All rights reserved.

investigated for crystal structures, spectroscopic investigations [20–26] , and computational studies, but title compound **Fmoc**-L-**Glu(OtBu)** has not been reported for spectroscopic studies or DFT calculations, to the best of my knowledge.

Since herein, this manuscript, the compound was structurally characterised by experimental spectroscopic techniques (FT-Raman & FT-IR), reactivity descriptor investigations (FMOs, Fukui, & MEP), and with help of computational calculations using DFT/B3LYP methodologies. Moreover, we determined the topological parameters of the compound to ensure that non-bonded interaction forces (H-bond, van der walls interactions, and so on) existed between chemical functionalities such as amine (NH), hydroxyl (OH), or carboxyl (COOH) groups. Also, molecular docking was performed with three different cancer cell development proteins, due to its significant importance in molecular biology and drug delivery of several diseases particularly cancer.

2. Experimental techniques

The chemical that is being investigated Fmoc-L-glutamic acid 5–tert–butyl ester ($C_{24}H_{27}NO_6$) in solid form procured from Alfa Aesar chemical company, and for the spectral analysis, it's been utilized without further purification. The FT-Raman spectrum of **Fmoc-L-Glu(OtBu)** was measured in the range of 4000–50 cm^{-1} using an FT-Raman spectrometer with a Bruker RFS27 with a resolution of up to 2.0 $cm^{-1}$and a source of light Nd: YAG laser with a 200 mW output power and 1064 nm range of laser; cooled Ge and liquid nitrogen was used as detectors. The FT-IR spectrum of **Fmoc-L-Glu(OtBu)** was recorded in the range of 450–4000 cm^{-1} using the PerkinElmer Spectrum-1 spectrometer, with up to 1.0 cm^{-1} resolution. A Jasco model with version V-670 spectrometer was used to investigate the chemical's UV absorption spectrum in the 400–200 nm range. The UV pattern was generated using a 10^{-5} molar solution of **Fmoc-L-Glu(OtBu)** in DMSO solvent. The reaction quickly scans at a speed of 2000 nm/min using the light source D2/WI.

3. Quantum computational calculations

The quantum computation employs the DFT with the standard B3LYP method with the 6-311++G(d,p) level to identify the optimized geometric structure of the **Fmoc-L-Glu(OtBu)** molecule, and this optimized structure, as well as the same DFT method, were used for all computational calculations that could be used in it. Gaussian 09 W package program [27] and Gaussview molecular visualization application were utilized for all these computations. Using AIM & Multiwfn.3.8 software [28,29], the topological analysis including ELF and LOL studies of the compound was done to ensure that non-covalent connections in the different solvent phases. In addition, the vibrational wavenumbers of the **Fmoc-L-Glu(OtBu)** molecule with the lowest energy were calculated in the vapor form. Wavenumbers ranging from 1700 to 4000 cm^{-1}, even those below 1700 cm^{-1}, were scaled using 0.958 and 0.983, respectively [30]. To characterize them, the PED contributions for frequencies of the al vibrations were computed using the VEDA tool [31]. To analyze the reactivity of the substance for the same optimized structure, the FMOs analysis**,** Electrostatic potential energy (ESP) map, and local chemical reactivity parameters of Fukui functions, are used [32–37] Also, the optical properties and stability of chemicals were computationally obtained by NLO and NBO calculations. The experimental results compared to the theoretically calculated electronic excitation in the UV-Vis spectrum with the TD-DFT method [38,39]. The targeted protein (PDB codes: 3PP0, 7EFJ, and 1OQA) is associated with tumor cells, and the AutoDock tool [40], and the PyMOL viewer were used to execute molecular docking.

4. Results and discussion

4.1. Structure of the Fmoc-L-Glu(OtBu)

The title molecule contains four segments of planar including the Fluorene group, amine group along with carbonyl, L-glutamic acid, and tert–butyl ester. The dihedral angles, bond angles, and lengths are major attributes of this molecular structure in which geometric parameters have been examined via the bonding strength, position, and chemical environments. The optimized structure of Fmoc-L-glutamic acid 5–tert–butyl ester (**Fmoc-L-Glu(OtBu))** was computed using DFT techniques and selected parameters are compared with experimental values acquired from [41] a similar molecule's crystallographic information as listed in Table S1 (supplementary material), and molecular structure with numbering scheme in the gas phase was shown in Fig. 1. The main torsion angles (e.g. C25-O1-C13-C8, O1-C25-N7-C18, O5-C31-C27-C24, and C23-O2-C26-C18) that determine the structural units of these segments can be seen in this diagram and Table S1 shows a few of them. The bond lengths and angles of **Fmoc-L-Glu(OtBu)** are consistent with those reported in the publications but the torsion angles slightly deviate from the given experimental results due to the little changes in chemical environments from reported compounds (e.g. the torsion angles C25-O1-C13-C8 & O5-C31-C27-C24 are -165.15 & -51.71in DFT and −125.55 & -63.60 in experimental, respectively).

The calculated parameters did not differ more than 0.148 Å (at N7-H47) of bond length and 2.91°(C15-C8-H32) of bond angle from the experimental results. The highest calculated intramolecular distance at C18-C24 & C13-C8 (1.549 & 1.529 Å) and this elongation are due to the largest molecular groups of Fluorene and L-glutamic acid bonded at C13 and C18, respectively, which also state that the weakest bonding between the atoms. The lowest bond distances were found at O3=C25, O4=C26, & O6=C31 (1.213, 1.208, & 1.207 Å) due to double bond attachments of carbonyl and carboxylic group, which shows that the strongest bonding between them. The title chemical's calculated N–C bond length (N7-C25=1.359 Å) is nearly identical to the literature results (1.344 Å). The largest bond angles (130.9, 129.3 & 129.2°) were identified at (C11-C12-C17, C8-C10-C15, & C8-C9-C14) Fluorene rings, this may be due to the delocalized electrons of two benzene rings interact with a five-membered ring of Fluorene in C=C bonds, ensure that these two ring systems' delocalized electrons to overlap. Hence this molecular group of **Fmoc** is a highly stable and protecting group. A significant deviation was found between the **Fmoc-L-Glu(OtBu)** O–C=O bond angles at C26, C25 & C31(O2-C26-O4=125.8°; O1-C25-O3=124.6°; O5-C31-O6=122.6°); at C26 and C25 have greater angles (∼2°) than C31, which can be due to lone pair interactions between the amine and carbonyl group molecules.

4.2. Topological analysis: non-covalent weak interaction predictions

The topological features of the title chemical **Fmoc-L-Glu(OtBu)** were investigated using the Multiwfn program and AIMAll software for the electronic structure, covalent and non-covalent weak interactions predictions by electron localization function (ELF), localized orbital locator (LOL), reduced density gradient (RDG) studies and atoms in molecules (AIM).

4.2.1. AIM

Several chemical processes are characterized using the AIM analysis, which focuses on structural aspects of electron density. The main objective of this study was to identify non-bonded weak interaction forces between chemical functionalities like amine (NH), hydroxyl (OH), or carboxyl (COOH) groups in gas and solvent phases. To define bond classifications, use the parameters p(r)

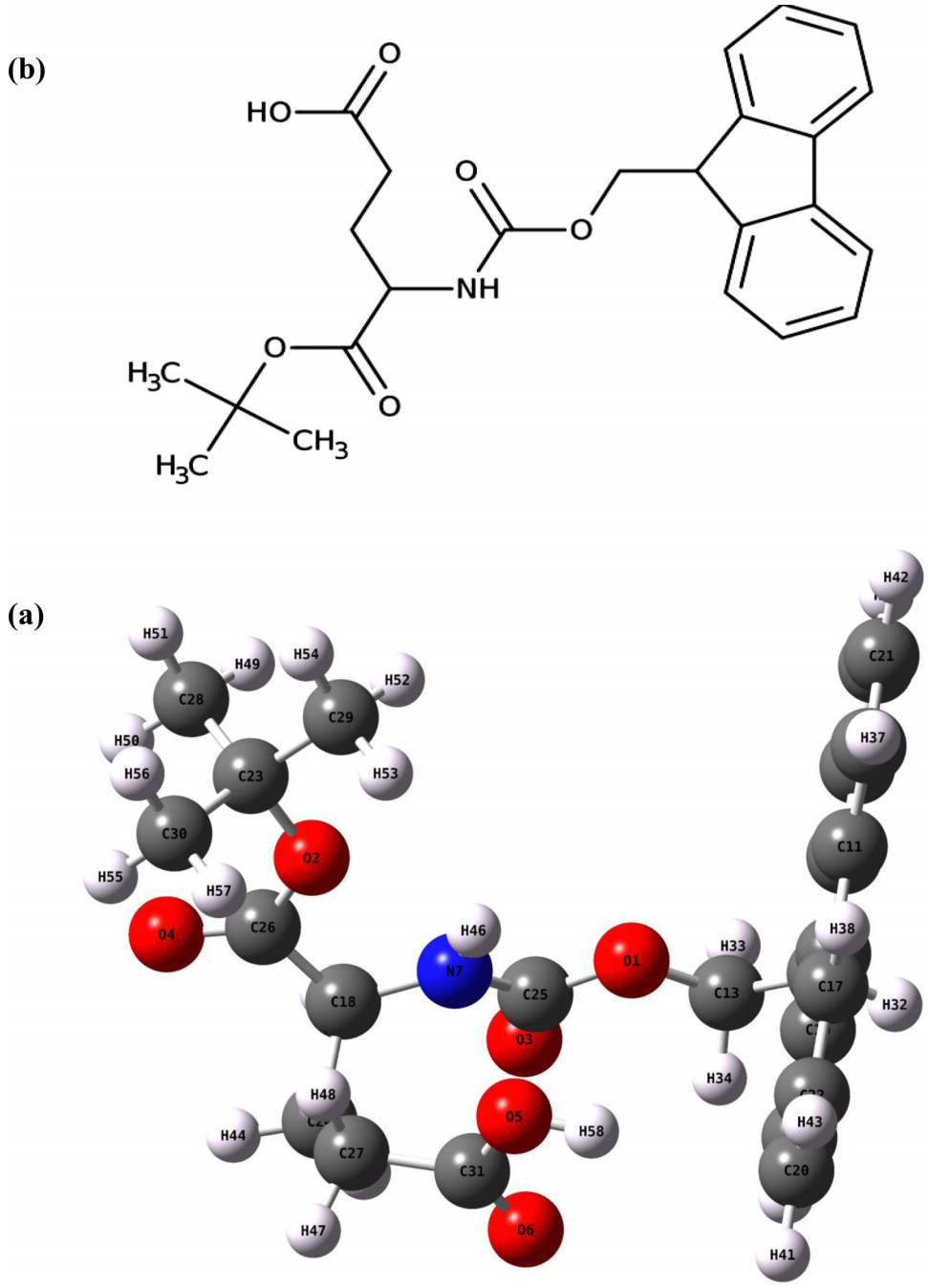

Fig. 1. Structure of the compound **Fmoc-L-Glu(OtBu)** (a) Optimized stable Structure in the gas phase (b) Chemical structure.

the electron density; ∇^2p(r) the IInd derivative electron density of Laplacian electron density; H (r) local energy density; G(r) & V(r) kinetic & potential energy density and it's the ratio of (G/V) [42,43]. In addition, interaction energy (ΔE_{HB}) and ellipticity (ε) can be used to determine the H-bond classification and asymmetry of the molecule. Table 1 lists the above-mentioned calculated non-boned weak interaction parameters of **Fmoc-L-Glu(OtBu)** in gas, water, DMSO, Et2O, and DMF, respectively. The AIM Molecular graphs of the compound with non-boned weak interaction are presented in Fig. 2(a–e) for gas, water, Et_2O, DMSO, & DMF, respectively. Table S2(a–e), provides, the topological parameters (all in a.u) at the bond critical point (BCP) of Fmoc-L-Glu(OtBu) [Electron density (ρ(r)), Laplacian of electron density ($\nabla^2\rho$(r)), Ellipticity (ε), Hamiltonian form of Kinetic energy density (K(r)) and distance (D, in Å) of Bond Path Length from the nuclear attractors] for gas, water, Et2O, DMSO, & DMF, respectively.

In the molecular system, Closed-shell (e.g. hydrogen contacts, electrostatic forces, van der Waals forces, etc.) and shared-shell (e.g. covalent bonds) interactions between BCPs are frequently distinguished using the parameters of electron density ρ(r) and Laplacian electron density $\nabla^2\rho$(r) In general, the calculated $\nabla^2\rho(r) < 0$ a.u. (or negative) values and p(r) $\geq$ 0.143 a.u. values showed that the shared covalent bond interactions while $\nabla^2\rho$(r) 0.1 a.u. and positive Laplacian electron density $\nabla^2\rho(r) > 0$ values are exhibited that the existence of the Van der Waals forces, weak hydrogen bond connections, etc., at BCPs. In the present case, the strongest

Table 1
Topological parameters of the Fmoc-L-Glu(OtBu) for non-covalent weak interactions in gas and solvent phases.

BCP	Length Å	ρ(r) (a.u)	$\nabla^2\rho$(r) (a.u)	V(r) (a.u)	G (r) (a.u)	H(r) (a.u)	-(G/V)	ε	ΔE_{HB} (kcal/mol)
				Gas					
C20…H58	2.578	0.0063	0.0269	−0.0037	0.0052	0.0015	1.4205	0.3002	−1.14
O6…C15	3.597	0.0021	0.0128	−0.0013	0.0022	0.0010	1.7629	1.9861	–
				Water					
O2…N7	2.576	0.0227	0.1114	−0.0257	0.0268	0.0011	1.0426	2.5555	–
C15…H58	2.574	0.0202	0.0616	−0.0139	0.0147	0.0007	1.0531	0.3864	−4.35
O4…H55	2.394	0.0131	0.0610	−0.0105	0.0129	0.0024	1.2242	0.5817	−3.29
O4…H50	2.423	0.0124	0.0576	−0.0098	0.0121	0.0023	1.2332	0.7187	−3.07
N7…C31	2.780	0.0167	0.0548	−0.0132	0.0135	0.0002	1.0183	0.7297	–
O2…H48	2.457	0.0109	0.0528	−0.0084	0.0108	0.0024	1.2858	0.6278	−2.63
O6…H34	2.497	0.0085	0.0432	−0.0060	0.0084	0.0024	1.4071	0.0825	−1.86
O6…H36	2.704	0.0062	0.0306	−0.0038	0.0057	0.0019	1.5048	1.0935	−1.19
O5…H53	3.430	0.0006	0.0050	−0.0003	0.0008	0.0005	2.5054	0.2474	−0.10
				Et_2O					
O2…H46	2.066	0.0258	0.1206	−0.0296	0.0299	0.0003	1.0091	0.7978	−9.26
O4…H55	2.395	0.0130	0.0602	−0.0104	0.0127	0.0023	1.2255	0.5598	−3.24
C15…H58	2.209	0.0186	0.0569	−0.0124	0.0133	0.0009	1.0735	0.5729	−3.88
N7…C31	2.789	0.0163	0.0533	−0.0127	0.0130	0.0003	1.0250	0.5283	–
O2…H48	2.481	0.0108	0.0520	−0.0084	0.0107	0.0023	1.2770	1.0418	−2.62
O4…H50	2.488	0.0109	0.0508	−0.0083	0.0105	0.0022	1.2643	1.1758	−2.60
O6…H34	2.481	0.0087	0.0446	−0.0063	0.0087	0.0024	1.3896	0.0784	−1.96
O6…H36	2.596	0.0077	0.0385	−0.0050	0.0073	0.0023	1.4624	0.6056	−1.56
O5…H53	2.742	0.0043	0.0232	−0.0022	0.0040	0.0018	1.8494	0.0524	−0.67
H48…H57	2.391	0.0047	0.0171	−0.0020	0.0031	0.0012	1.5854	0.3736	–
				DMSO					
O2…N7	2.576	0.0227	0.1114	−0.0257	0.0268	0.0011	1.0425	2.5347	–
C15…H58	2.158	0.0202	0.0615	−0.0139	0.0146	0.0007	1.0536	0.3839	−4.35
O4…H55	2.394	0.0131	0.0609	−0.0105	0.0129	0.0024	1.2244	0.5826	−3.29
O4…H50	2.424	0.0124	0.0576	−0.0098	0.0121	0.0023	1.2334	0.7203	−3.07
N7…C31	2.780	0.0167	0.0548	−0.0132	0.0135	0.0002	1.0183	0.7278	–
O2…H48	2.457	0.0109	0.0528	−0.0084	0.0108	0.0024	1.2859	0.6320	−2.63
O6…H34	2.497	0.0085	0.0433	−0.0060	0.0084	0.0024	1.4066	0.0826	−1.87
O6…H36	2.700	0.0062	0.0308	−0.0038	0.0058	0.0019	1.5045	1.0686	−1.20
O5…H53	3.427	0.0006	0.0050	−0.0003	0.0008	0.0005	2.5035	0.2407	−0.10
				DMF					
O2…N7	2.539	0.0227	0.1114	−0.0257	0.0268	0.0011	1.0425	2.5594	–
C15…H58	2.209	0.0202	0.0615	−0.0139	0.0146	0.0007	1.0538	0.3853	−4.34
O4…H55	2.395	0.0131	0.0609	−0.0105	0.0129	0.0024	1.2244	0.5832	−3.29
O4…H50	2.488	0.0124	0.0576	−0.0098	0.0121	0.0023	1.2332	0.7184	−3.07
N7…C31	2.789	0.0167	0.0548	−0.0132	0.0135	0.0002	1.0182	0.7238	–
O2…H48	2.481	0.0109	0.0528	−0.0084	0.0108	0.0024	1.2858	0.6313	−2.63
O6…H34	2.481	0.0085	0.0433	−0.0060	0.0084	0.0024	1.4063	0.0826	−1.87
O6…H36	2.596	0.0062	0.0309	−0.0038	0.0058	0.0019	1.5038	1.0590	−1.20
O5…H53	2.742	0.0007	0.0050	−0.0003	0.0008	0.0005	2.5013	0.2357	−0.10

covalent bonds are found form the Table S2(a–e) with the negative $\nabla^2\rho$(r) and positive ρ(r) values in solutions and gas phases (e.g. in the gas phase, the BCPs of O6-C31 p(r) = 0.3688 and ∇^2p(r) 0.1185). For the gas phase, the highest electron density was found at BCP O6-C31; however, for all solvent phases, it was shifted at BCP O4-C26. Table 1 summarises the weak non-covalent connections for all media, demonstrating that the **Fmoc-L-Glu(OtBu)** was stabilized in the liquid phase with more weak contacts than in the gaseous form. Only two non-bonded connections were detected in the gas phase (at C20...H58 and O6...C15 with distances of 2.578 and 3.597), but the number of weak contacts increased significantly in the solvent phases at BCPs O2...N7, C15...H58, O4...H55, O4...H50, N7...C31, O2...H48, O6...H34, O6...H36, O5...H53 for water, DMSO, & DMF. Among the interactions listed above, only the O2...N7 contact was not identified in the DMF, whereas the O2...H46 and H48...H57 are additionally present in this solvent. The Hydrogen bond connections (C15...H58, O4...H55, O4...H50, O2...H48, O6...H34, O6...H36, & O5...H53) for all media were detected weak; electrostatic and non-covalent nature by the positive local energy and Laplacian electron densities (: for weak Hydrogen bonds $H(r) > 0$ &$\nabla^2\rho(r) > 0$) [44]. The hydrogen bond interaction energy was also calculated and the greatest interaction was found at O2…H46 for DMF; C15…H58 for water, DMSO, and DMF solvents.

4.2.2. ELF and LOL

In the molecular structure, bonding and antibonding electrons (e.g. covalent bonds, lone pairs) may be visualized using the localized orbital locator (LOL) and the electron localization function (ELF) based on electron density attributes. The value of ELF varies between 0.0 and 1.0, while LOL was 0.0 to 0.8 (with color interpretation ranging from blue to red), with considerably large values implying regions with localized electrons attributed to the existence of a sharing of electrons (covalent bond) and electrons of lone pairs, and their smaller values denoting regions where electrons are anticipated to be delocalized [45]. In the current study, the electronic structure of **Fmoc-L-Glu(OtBu)** ELF and LOL maps are obtained in both solvent and gas phases and shown in Fig. 3(a–c), respectively. Electron delocalization and localization are expressed by the colours blue and red, accordingly. The deepest red zones are seen at the hydrogen atoms of H55, and H37 in water, DMSO, and DMF solvents; H53, and H38 for Et_2O are shown in these Figures, whereas the area with the deepest blue was seen at C28, O2, C27, C21, C11, C10, & C15 through gas phase and it was reduced in solvent phases only can be seen at C23 for water, DMSO, and DMF; at C13 for Et_2O. They also concluded that the highest possible delocalization sites with chemical environments at C16-C21-C19 & C10-C15-C20 for gas-phase; C8-C13-O1 for Et_2O; and C30-C23-C29 for water, DMSO, & DMF by the deepest blue circles at C21, & C15, (for

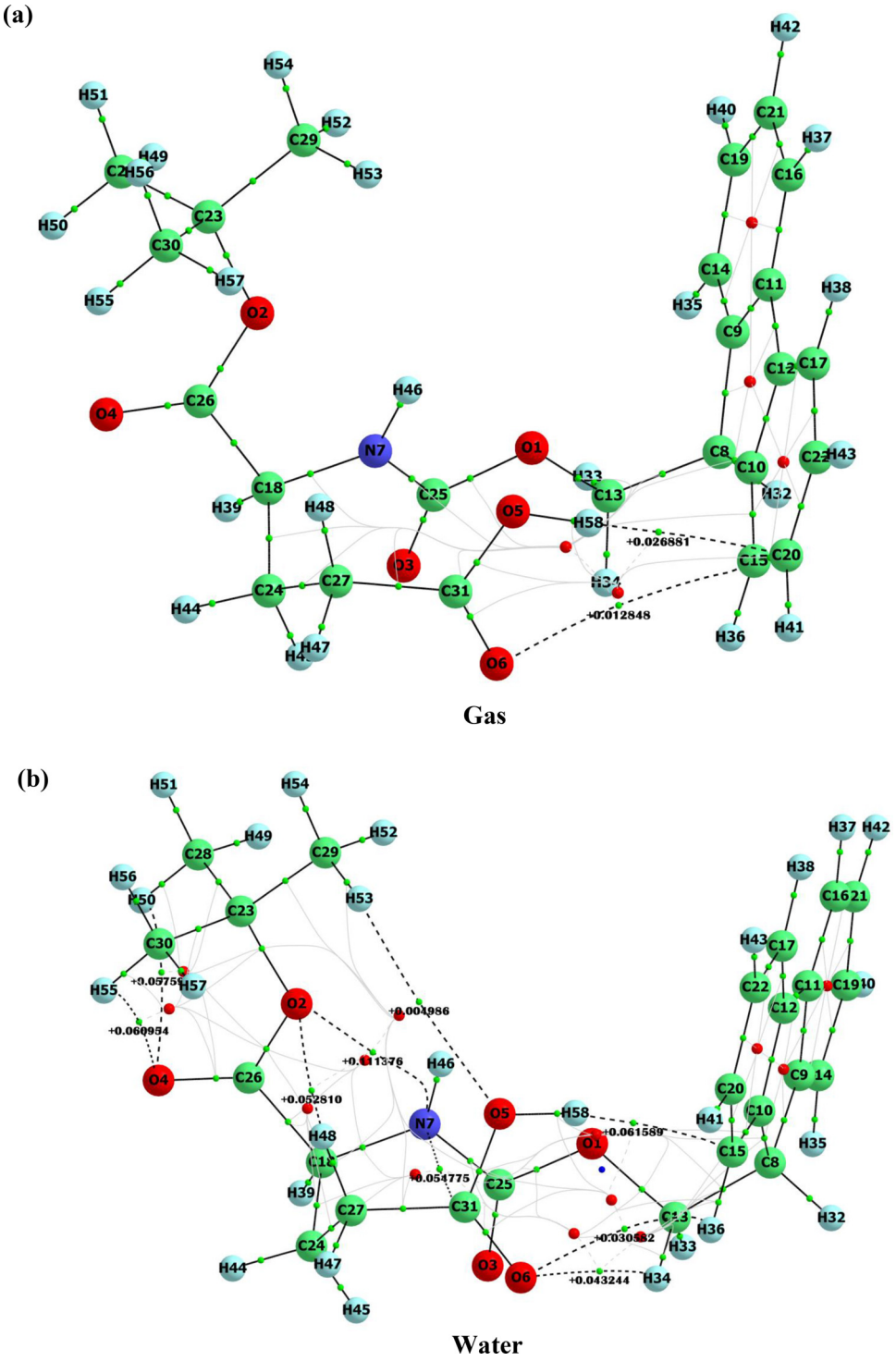

Fig. 2. AIM Molecular graph of **Fmoc-L-Glu(OtBu)**: green tiny spheres (BCPs), small red sphere (RCBs), black lines (bond paths), ash color solid lines (RCP to BCP ring path), and black dotted lines (Non-covalent interactions (NCI)) with Laplacian electron density $\nabla^2\rho(r)$ values are illustrated in these figures.

gas) C13 (for Et2O) & C23 (for water, DMSO, & DMF) on the **Fmoc-L-Glu(OtBu)**, and their 3D ELF map with electronic environments are given in Fig. 4(a–d).

4.2.3. RDG

RDG Non-covalent contact analysis is an enhancement of the AIM study and is being used to detect weak interactions in the structure with its environment, such as attractive van der Walls and H-bonds interactions and repulsive steric effect. NCI information is required to characterize the biological affinity and disinclination regions of the **Fmoc-L-Glu(OtBu)** structure, which is also subjected to chemical stability, molecular identification, self-assembly, re-crystallization, and molecular docking. The RDG function, which is depicted below, is an electron density gradient without dimension form [46],

$$RDG = \frac{1}{2\left(3\pi^2\right)} \frac{|\nabla\rho(r)|}{\rho(r)^{4/3}} \quad (1)$$

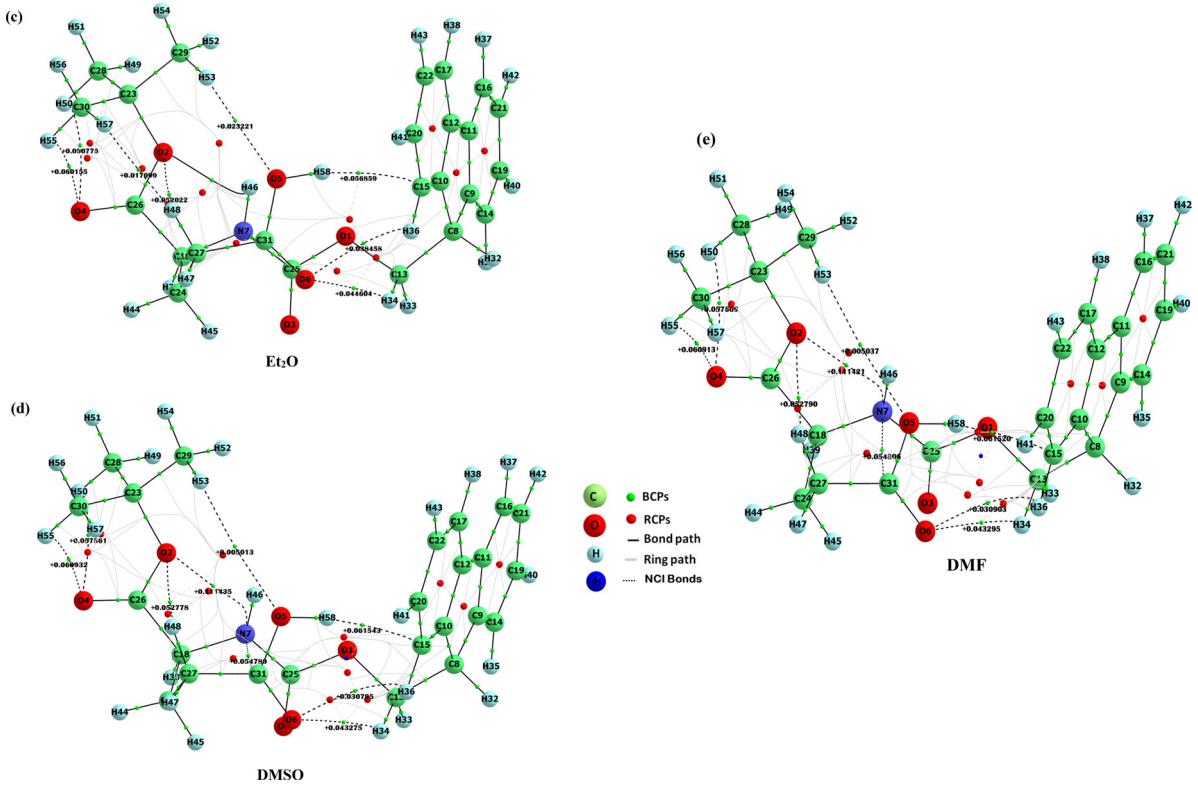

Fig. 2. Continued

In this work, the RDG maps were carried out in different media of gas, water, Et_2O DMSO, and DMF for weak interaction predictions and are shown in Fig. 5(a–e). Using Eq. (15), with the electron density$\rho(r)$ was RDG map picturized in the small region of the spectrum between positive values and negative values of sign $(\lambda_2)\rho$. This color spectrum represents molecular attractive (non-covalent), repulsive (steric), and neutral (van der Walls) interactions by blue, red, and Green regions. In the compound **Fmoc-L-Glu(OtBu)** in the gas phase, there is no non-covalent region was found but strong repulsive steric and van der walls interactions are detected by red (at 0.01, 0.02, & 0.038 a.u.) and green (at 0.00, −0.01, & −0.02 a.u.) spikes, respectively. On the RDG maps of water, DMSO, Et_2O, and DMF solutions, the non-covalent contact of the title chemical in the solvent phase was seen at bellow 0.002 a.u. by blue and dark green color areas, notably strongly shown (at about −0.026 a.u.) in Et_2O solvent. This finding is in agreement with AIM data of weak interactions seen only in the solvent phase.

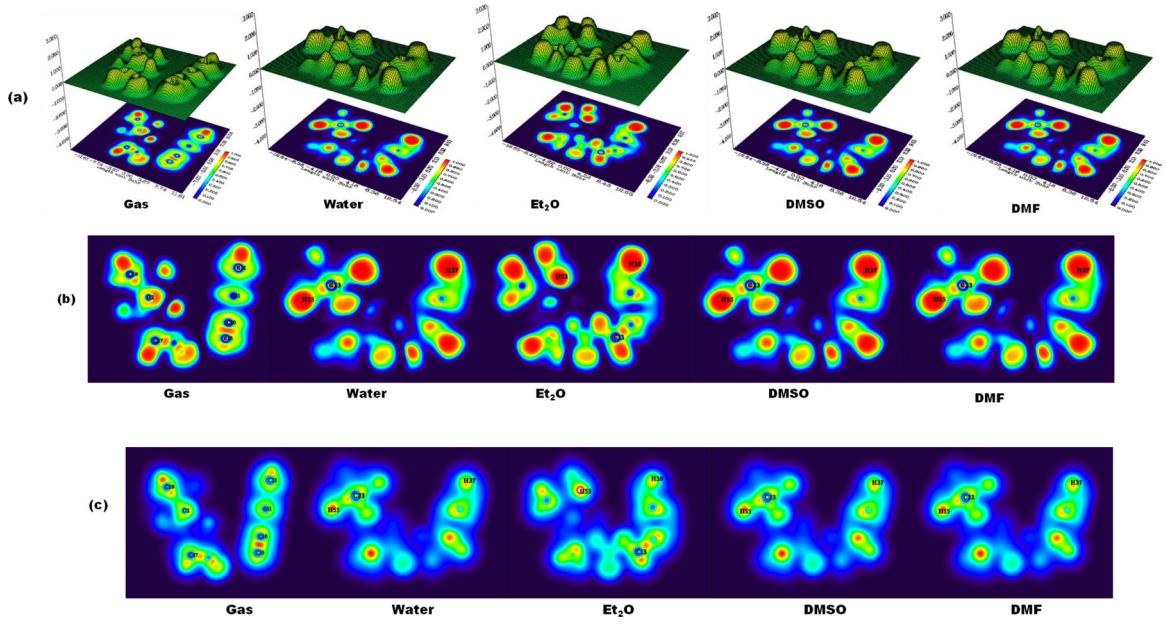

Fig. 3. (a) 3D Electron localization function (ELF) map with chemical environments (b) Electron localization function (ELF) maps and (c) Localized orbital locator (LOL) maps **Fmoc-L-Glu(OtBu)**, in the gas and solvent phases.

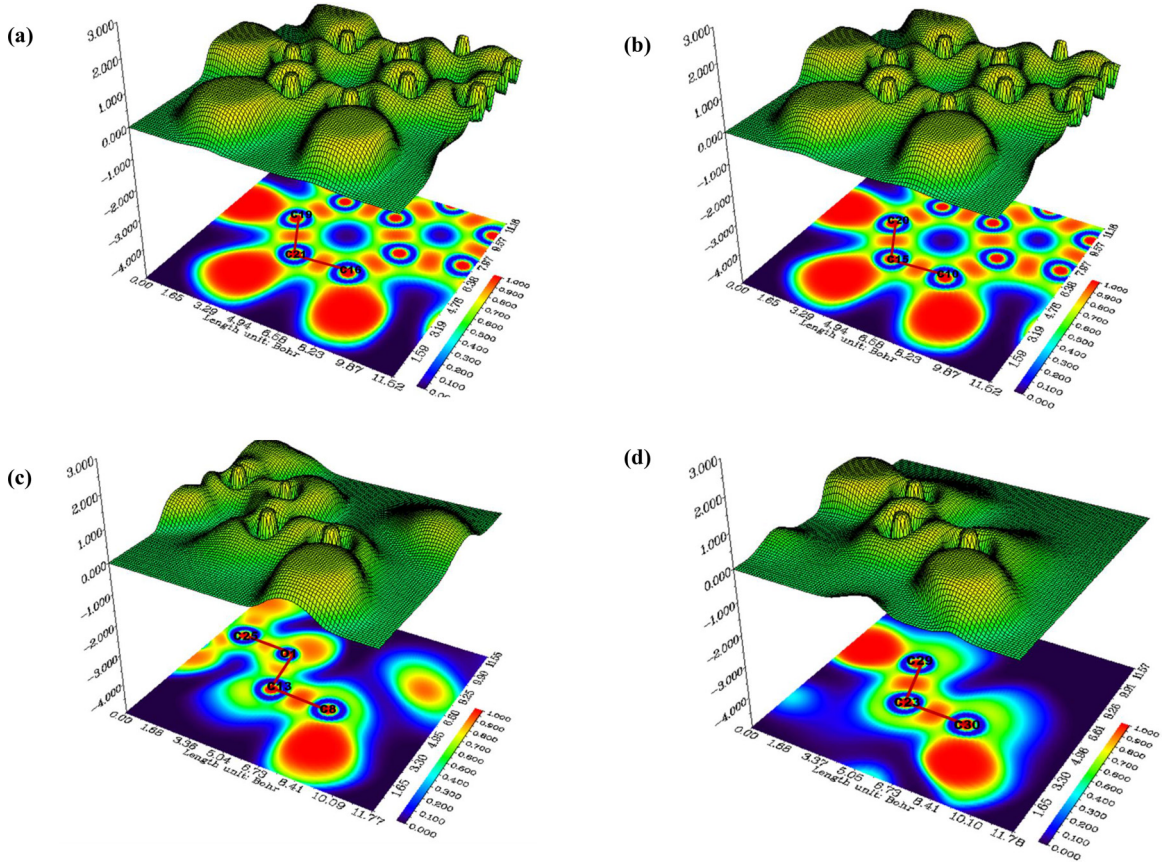

Fig. 4. The ELF map with an electronic environment shows that the highest delocalization regions of (a) C16-C21-C19 & (b) C10-C15-C20 in gas-phase; (c) C8-C13-O1 in Et_2O; and (d) C30-C23-C29 for water, DMSO, & DMF solvent of **Fmoc-L-Glu(OtBu)**.

4.3. Structural characterization: vibrational assignments

Vibrational spectra are one of the most effective tools for analyzing the molecular structure and functional group conformational studies in organic molecules. The title chemical Fmoc-L-glutamic acid 5–tert–butyl ester, has a Fluorene group (two benzene rings), amine group along with carbonyl, L-glutamic acid, and tert–butyl ester and it consists of important molecular groups of amine (NH), hydroxyl (OH), or carboxyl (COOH) groups and CH_2, CH_3 along with two benzene rings. As per DFT optimization with vibrational study results, there are 168 vibration modes in all, and the Gaussview tool was used to predict the fundamental modes of vibrations. The

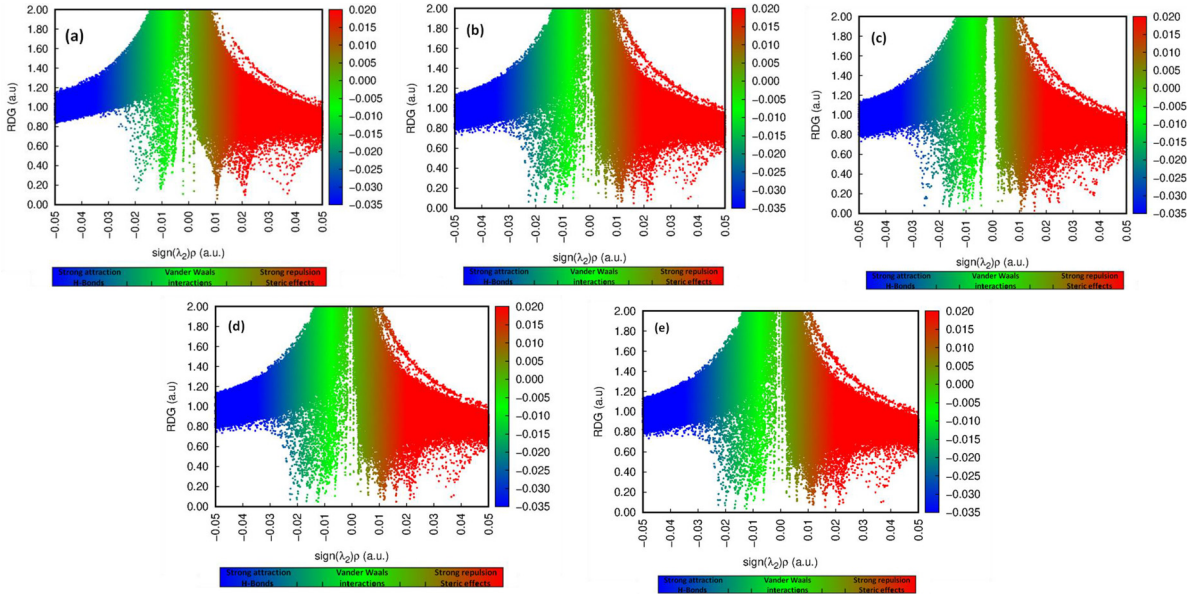

Fig. 5. RDG Plots versus the electron density ρ multiplied by the sign of λ_2 of the title compound in (a) Gas (b) Water (c) Et_2O (d) DMSO & (e) DMF phases.

frequency lower than 1700 cm^{-1} was scaled with 0.983, whereas the frequency between 1700 and 3500 cm^{-1} was scaled with 0.958 [30]. In Figs. S1 and S2 (Supplementary materials), the comparison of experimental (FT-IR & FT-Raman) and theoretical vibrational IR and Raman spectra of the **Fmoc-L-Glu(OtBu)** are displayed. Table S3 lists Vibrational frequencies with assignments, IR intensities (I_{IR}), and Raman scattering activities (SA_{Raman}) of **Fmoc-L-Glu(OtBu)** in the gas phase and compared with experimental FT-IR and FT-Raman frequencies.

Carboxylic acid produces high-intensity bands during vibrations due to its typical frequencies, which include stretching vibrations of hydroxyl (OH) and carbonyl (C=O). The stretching frequency O–H is identified by a band that emerges in the 3400–3600 cm^{-1} range [47]. The peaks of these bands are noticeably higher and wider than the amine stretches that arise in the same region. In this case, the strong FT-IR intensity band was observed at 3520 cm^{-1} and a very strong band at 3507 cm^{-1} for the FT-Raman spectrum while the calculated wavenumbers at 3514 cm^{-1} for pure O–H stretching due to 100% PED contributions. The C=O stretching was particularly prominent in the infrared spectrum because molecules form exceptionally broad and strong bands due to IR ray absorption. The stretching vibrations of the C=O methyl ester group and carboxylic's acid and more likely to range between 1790 and 1660 cm^{-1} [48,49]**.** In this instance, the C=O stretching of carboxylic's acid, Ester group and carbonyl (nearby NH) were found at 1727, 1704 & 1702 cm^{-1} in DFT with PED percentage of 88, 90, & 87, respectively; they were experimentally measured at 1728 (strong), 1708 (very strong) & 1696 (very strong) for FT-IR and at 1730 & 1703 cm^{-1} for FT-Raman. The CO strong absorption bands due to stretching in IR frequency is among the characteristics of carboxylic acid, and it was detected in this case using a strong FT-IR intensity band at 1259 and 1085 cm^{-1}; FT-Raman at 1249 cm^{-1}; and related computed wavenumbers at 1266 and 1074 cm^{-1}. The amine (NH) group stretching vibration arises generally at 3450–3250 cm^{-1} **[**50]. Protonation affects the stretching of the N–H bond because the bands associated with N–H stretching mode are shifted to a higher region. In this instance, it was detected at 3483 cm^{-1}(strong intensity) for FT-IR; 3493 cm^{-1} (very strong) for FT-Raman; and estimated scaled wavenumber at 3490 cm^{-1} for practically pure NH vibration because 89 percent of PED value was derived for this region. The title compound has one CN covalent bond in this instance, the characterization of C–N stretching frequencies in a molecule is a challenging task due to difficulties distinguishing these frequencies from other vibrations. C–N stretching is typically found in the 1400–1200 cm^{-1} range [51]**,** and its stretching mode was calculated at 1074 cm^{-1}; the strong IR intense band at 1085 cm^{-1}.

Usually, the methyl (CH_3) group molecules are considered to have nine major vibrational modes (3 stretchings; 5 bendings; 1torsion). Expected literature CH_3 vibrations regions are in 2935–2860 cm^{-1} for CH_3 asymmetric stretching; in 2985–2925 cm^{-1} for CH_3 symmetric stretching; at & 1020–930 cm^{-1} & 1080–1020 cm^{-1} regions of CH_3 rocking; less than 400 cm^{-1} shows for CH_3 torsion [52]. In this instance, the asymmetric stretching of CH_3 were detected at 3008, 3006, 2980, 2980, 2968, 2967, 2966, & 2965 cm^{-1} and their PED values (100%, 98,% 100%, 100%, 98%, 100% , 58%, & 58%) demonstrate that the pure CH_3 asymmetric stretching mode was assigned**.** These asymmetric CH_3 frequency bands are seen at 2975 & 2963 cm^{-1} for FT-IR and very strong intensity bands measured at 3001, & 2968 cm^{-1}. Similarly, the pure CH_3 symmetric vibrations were calculated at 2916, 2909 & 2908 cm^{-1} with 98, 100, and 100 PED contribution percentages, respectively. Experimental FT-Raman and FT-IR spectrums have been recorded at 2906, 2911 cm^{-1}. The CH_3 bending vibrations also were determined by calculating, and the scaled frequencies are presented in Table S3 in the following regions: 1502–1447 cm^{-1} (scissoring); 1406–1378 cm^{-1} (wagging); 1257–1246 cm^{-1} (twisting); 1164–256 cm^{-1} (rocking); the four CH_3 torsions were calculated at 239, 253, 252, & 200 cm^{-1}, and they are strongly correlated with experimental and expected literature data. In general, the CH_2 group molecule has six basic vibrational (2stretching + 4bending) modes. Asymmetric stretching of CH_2 vibrations arises between 2900 and 3000 cm^{-1} [53], whereas symmetric CH_2 stretching vibrations can be seen at 2900–2800 cm^{-1} [54]. In this present work, asymmetric stretching of CH_2 was measured by FT-IR at 2963 cm^{-1}; at 2968 cm^{-1} with the strong band in FT-Raman. The computed DFT wavenumber of asymmetric CH_2 stretching was obtained at 2983, 2966, and 2965 cm^{-1}, correspondingly, with PED contributions of 96, 100, 58, and 58. The CH_2 bending vibrations also were estimated by DFT, and the scaled frequencies are presented in Table S3 in the following bands: at 1511–1452 cm^{-1} (scissoring); 1384–1364 cm^{-1} (wagging); 1322–1122 cm^{-1} (twisting); 1033–237 cm^{-1} (rocking); They also have a good correlation with experimental and expected reported values.

The ring C–C and C=C stretching vibrations were quite noticeable and incredibly characteristic vibrations in the aromatic ring band, and they are the most abundant region in the 1650–1400 cm^{-1} [55]. In this instance, the stretching of the aromatic quadrant of C=C was estimated at 1618, 1616, 1594, and 1588 cm^{-1} by DFT; and it was recorded at 1622, 1608 & 1581 cm^{-1} by FT-Raman spectra (not seen in FT-IR). At the same time, the semicircle C=C stretching mode was computed at 1483, 1482, 1455, 1451, & 1354 cm^{-1} and that was experimentally recorded by FT-IR at 1488, 1452, 1354 cm^{-1} with strong medium intensity bands; by FT-Raman at 1445, & 1350 $cm^{-1}$with weak and moderate bands.

Table 2
Calculated FMOs energy values of title compound by using B3LYP/6-311++G(d,p).

Global energy descriptor	Calculated Energy B3LYP/6-311++G(d,p) (eV)
HOMO (E_{HOMO})	−8.925
LUMO (E_{LUMO})	−5.180
Energy gap (ΔE)	3.745
Ionization potential (I_P)	8.925
Electron affinity (E_A)	5.180
Global hardness (η)	1.873
Global softness (S)	0.267
Electronegativity (χ)	7.053
Chemical potential (μ)	−7.053
Electrophilicity index (ω)	13.282
Nucleofugality (ΔE_n)	18.462
Electrofugality (ΔE_e)	22.207

4.4. Frontier molecular orbitals (FMOs) analysis

Chemical stability and reactivity are essential characteristics in molecular research, especially in organic chemistry and the medicinal area. According to many studies, the HOMO-LUMO (Frontier Molecular Orbitals) calculations accurately produce the electron donor and acceptor quantities [56]. A theoretical approach was used to study and report on HOMO-LUMO analysis for the gas state in this article**.** According to this study, the calculated HOMO energy −8.925 eV, and LUMO is −5.180 eV, with a narrow energy gap of 3.745 eV is shows that more reactive and has stability of **Fmoc-L-Glu(OtBu)** in the gas phase and it was shown in Fig. 6, and other parameters of global reactivity such as electron affinity (E_a), ionization potential (I_p), Global hardness (η), chemical potential (μ), softness (s), global electronegativity (χ), and electrophilicity index (ω) were utilized to more characterized of the chemical using DFT approaches and are listed in Table 2. The chemical's electron affinity value of 5.180 eV represents the rate of electron acceptability, whereas the ionization value of 8.925 eV implies the amount of

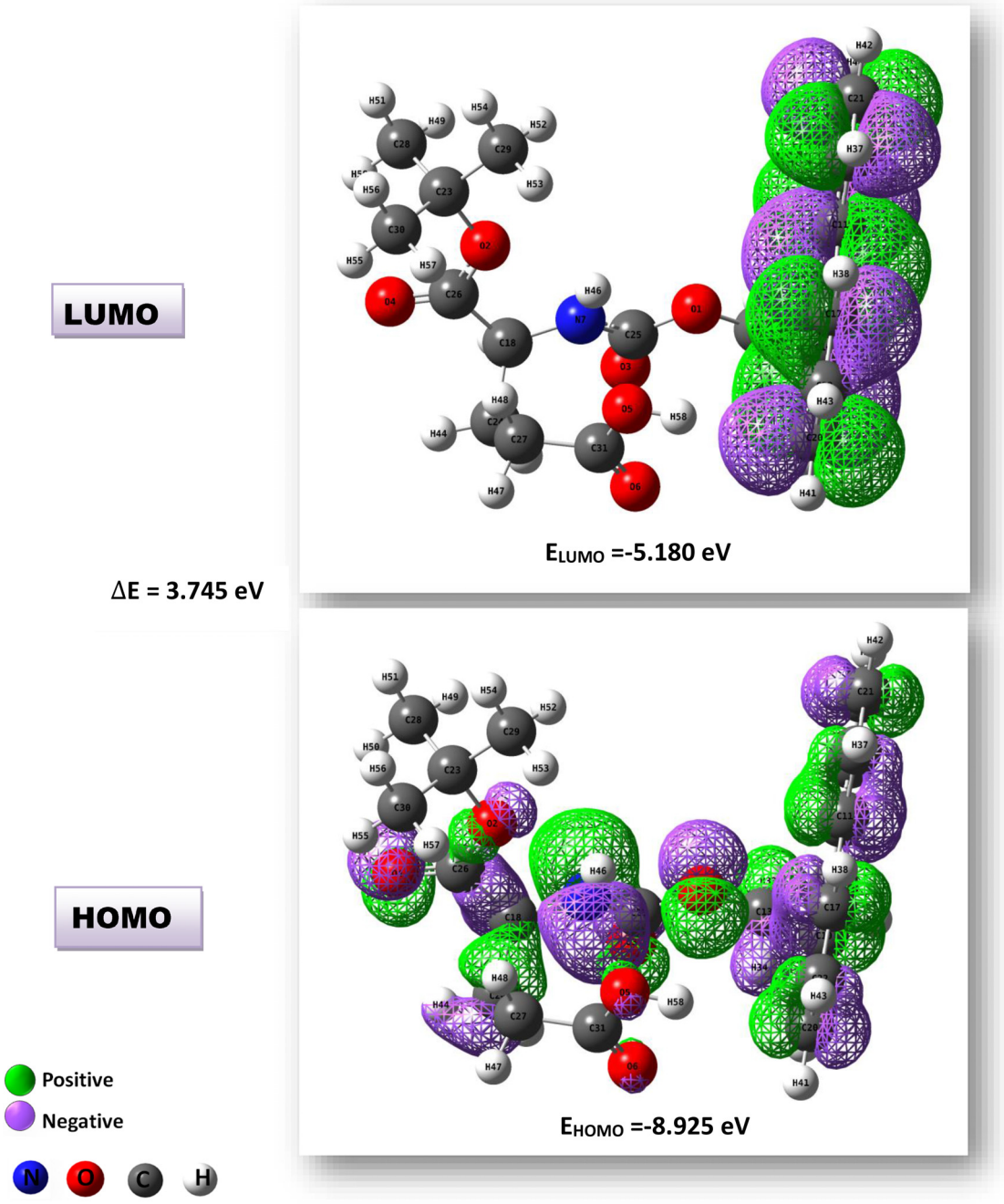

Fig. 6. The Frontier molecular orbitals (HOMO & LUMO) in the gas phase of the title compound.

effort consumed to remove electrons from higher most occupied orbitals, and the chemical softness value of 0.267 eV suggests that the chemical's poor toxicity.

4.5. Fukui functions analysis with NPA charge

The charges on the atoms of the **Fmoc-L-Glu(OtBu)** are assessed utilizing B3LYP functional by applying the natural population analysis (NPA) approach [57], and the results of Condensed Fukui functions (f^+, f^-, f^0 & Δf) and Local softness (sr^+ fr^+, sr^- fr^-, & sr° f^0) of **Fmoc-L-Glu(OtBu)** for gas with NBO charges were listed in Table S4 with the appropriate plot shows condensed Fukui functions (f^+, f^- & f^0) in Fig. S3. Except for C9 and C10, all other carbon atoms in two benzene rings produce negative charges. Due to strong double bond interactions on the title compound, carbon atoms at C25, C26, and C31 also exhibited negative charge; nevertheless, the larger negative values were detected at O5. The Fukui function parameters are derived from either the NBO or Mulliken charges but in this case obtained by NBO charges. The appearance of negative results of the Fukui function is shown in Table S4. A minus Fukui function value indicates that when an electron is added to a compound, the electron density is lower in certain areas; conversely, whenever an electron is withdrawn from the compound, the electron density is raised in certain areas. The electrophilic case's reactivity order was determined using the computed values. From this table, the electrophilic reactivity sequence was determined using the computed values are C11>C21> C19> C16> C9 >C20 > C12 > C22 >N7 >H42 >O4 etc.; and sequence atoms for nucleophilic attack are H58 >C19 >C16 >C17 > C20 > H47 > H54 > C14> C15 > H53 > C12 etc. These findings suc-

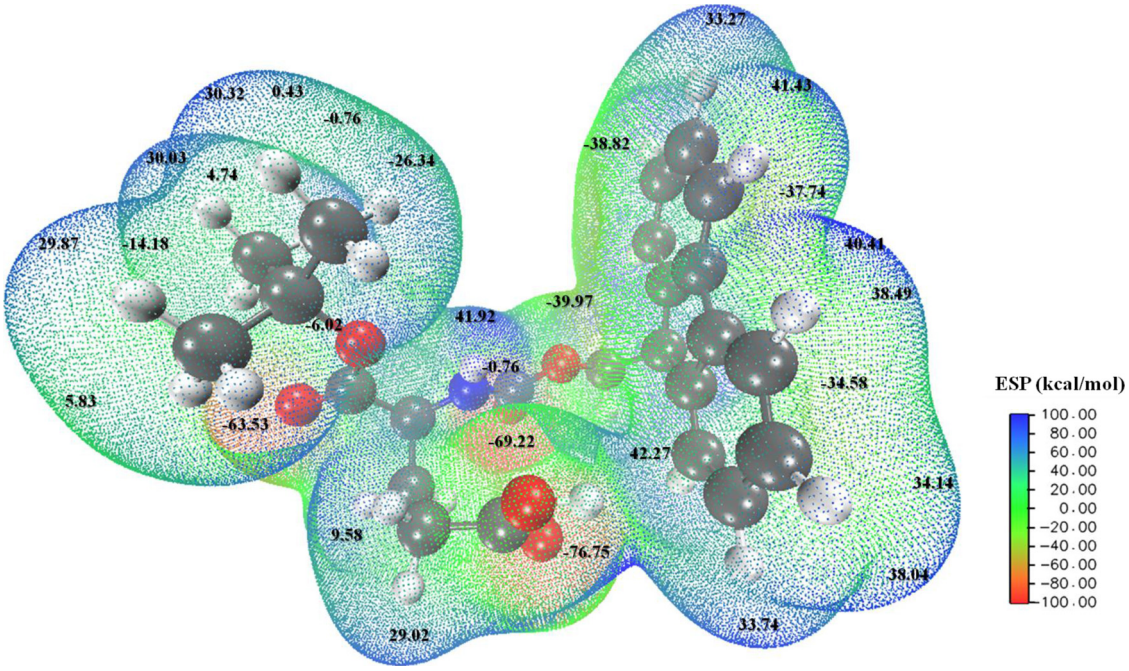

Fig. 7. Electrostatic Potential (ESP) surface map of **Fmoc-L-Glu(OtBu)**.

cessfully demonstrated the biological active region's involvement in docking research.

4.6. ESP surface analysis: reactivity sites predictions

The electrostatic potential (ESP) is a well-known method for investigating physical/chemical reaction zones, in molecular modeling research. It depicts the electrostatic potential in proportion to the molecule's electronic density graphically. A molecule's Electrostatic Potential is created by a system of nuclei and electrons. In the Born-Oppenheimer approximation, nuclei are allowed to treat as static positive ions (Z_A) located at R_A. However, because electrons are not stable, the average amount of electrons in a volume is referred to as the electronic density function $\rho(r)$. Since the electrostatic potential V(r) is expressed in terms of the atomic unit as [58].

$$V(r) = \sum \frac{Z_A}{|R_A - r|} - \int \frac{\rho(r')dr}{|r' - r|} \quad (2)$$

The different amounts of electrostatic potential energy on the surfaces of the ESP map are predicted by a color spectrum, with blue indicating the most electrostatic potential energy and red indicating the minimum number of molecules. The strongest repulsion and attraction are reflected in the dark red (negative) and dark blue (positive) portions, respectively. In the range of ESP energy −100 to 100 kcal/mol (deepest red to deepest blue), the electron density on MEP surfaces is shown in Fig. 7. Positive regions of blue-colored zones seem to be over Hydrogen atoms of CH_2, & CH_3 groups and benzene rings while the deepest blue color (42.27 kcal/mol) around the CH_2 (nearby benzene rings) of the title compound, whereas negative regions oxygen atoms (O3, O6, & O4) are at the carboxylic and carbonyl groups (COOH, CO, & C=O) while the darkest red color (−76.75 kcal/mol) was found at O3 of carboxylic acid group of the **Fmoc-L-Glu(OtBu)**. In comparison to other parts of the ESP surfaces, the green color sections, which equate to half potential among the deepest blue and red color areas, have practically neutral potential. Since the order of highest electron density was identified as O3>O6>O4>O1 etc., (order lowest electrostatic energy −76.75, −69.22 & −63.53 kcal/mol) shown by the darkest red colors.

4.7. Ultra violet-visible absorption spectra

UV–Vis spectroscopy studies of the **Fmoc-L-Glu(OtBu)** were carried out in the solvent and gas phases using the TD(time-dependent)-DFT technique [59], and the experimental UV absorption spectrum in the DMSO liquid phase was taken between 200 nm and 800 nm. Table 3 shows the energies of vertical excitations with absorption peaks (λ_{max}) calculated using the Linear Response approximation. The highest (259.60 & 259.44 nm) absorption maxima (λ_{max}) with oscillatory strength (f) of 4.777 & 4.780 were computed for Benzyl alcohol & Benzonitrile solvents due to HOMO→LUMO major transition with 87% contributions of the compound **Fmoc-L-Glu(OtBu)** this table lists the absorbance peak, transitions, and primary and secondary contributions including all solvents, as well as the theoretical spectra of UV-Vis absorptions for all media and, are shown in Fig. 8. In the experimentally measured spectra, the absorption maximum is seen at 283.33 nm. The predicted wavelengths correlate with the experimental measurement value, as shown in Table 3. This table reveals that there are three possible electronic transitions that led to the electronic verticals in the first excitation level: HOMO to LUMO, HOMO-3 to LUMO, and HOMO to LUMO+1. Those electronic excitations were depicted in Fig. 9. The HOMO is clearly noticeable in the oxygen (O1, O2, O3, O4, O5, & O6) and nitrogen (N7) atoms of lone pair electrons and the aromatic region of two benzene rings in this figure, while the LUMO is only viewable in the aromatic regions of two benzene rings.

4.8. Effect of solvent parameters on the UV-Vis spectra of Fmoc-L-Glu(OtBu)

The effect of polar solutions and non-polar solutions on numerous spectroscopic features of the molecule was adequately explained using solvent parameters. The polarity scale was used to analyze the **Fmoc-L-Glu(OtBu)** absorption maxima in several solutions in this case. The following relationship was used to trans-

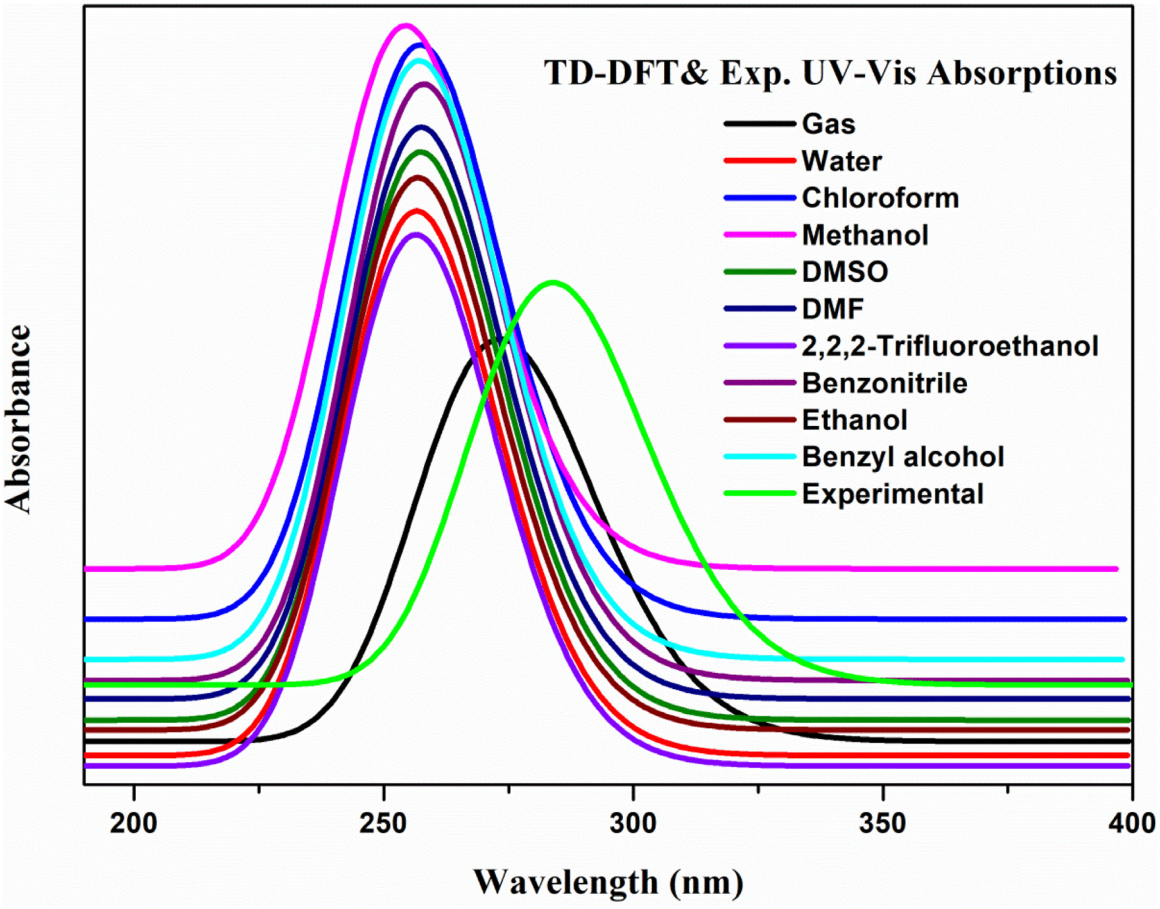

Fig. 8. The UV-Visible absorption spectrum of experimental and theoretical TD-DFT spectra for different mediums.

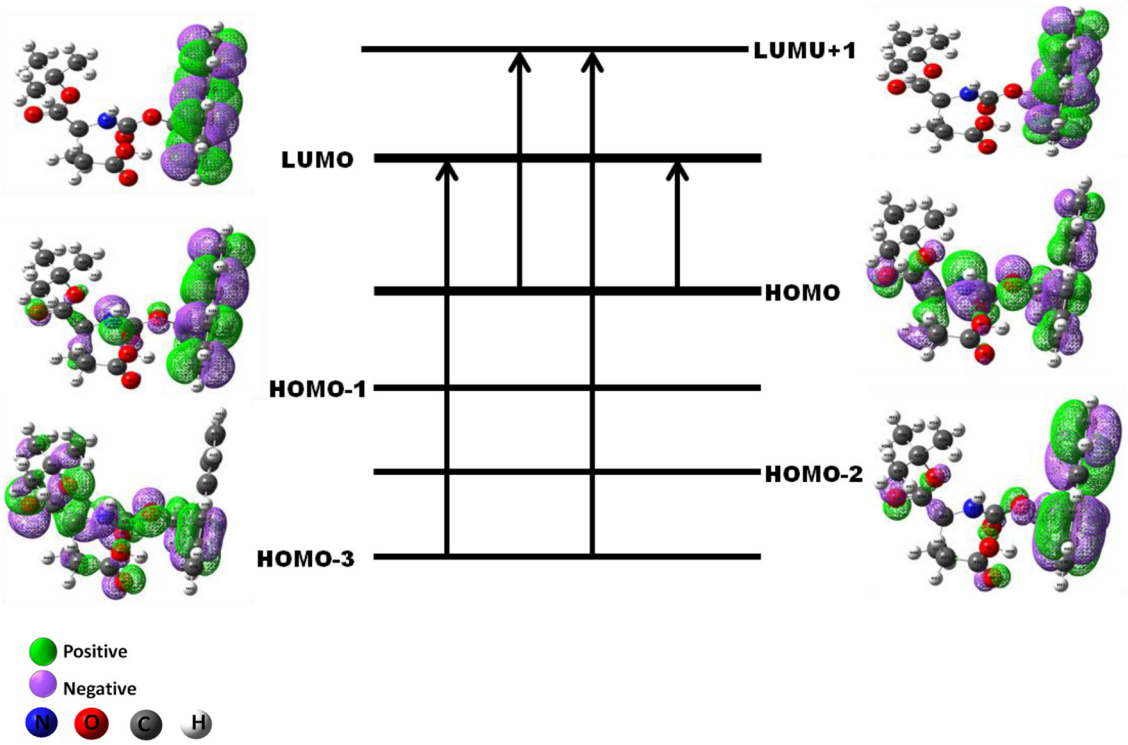

Fig. 9. Major four Electronic excitations due to L(n)→ $\pi*$ and $\pi \rightarrow \pi*$ transitions in the first excitation state with MOs diagrams of **Fmoc-L-Glu(OtBu)**.

Table 3
Electronic excitations of Fmoc-L-Glu(OtBu) obtained by experimental and TD-DFT/B3LYP/6-311++G(d,p) methods.

Medium	Experimental		TD-DFT/B3LYP/6-311++G(d,p)				Major and minor contributions[a]
	λ_{max} (nm)	Band gapΔE (eV)	λ_{max} (nm)	Band gapΔE (eV)	Energy (cm^{-1})	Oscillator Strength (f)	
Gas			277.95	4.461	35,977	0.1883	H ® L (53%) H ® L+1 (32%) H-3 ® L (9%) H-3→L+1(2%)
Chloroform			259.34	4.781	38,559	0.4690	H ® L (86%) H-3 ® L (4%) H →L+1 (5%)
Methanol			258.19	4.803	38,732	0.4330	H ® L (83%) H-3 ® L (6%) H →L+1 (6%)
Water			258.17	4.803	38,735	0.4350	H ® L (84%) H-3 ® L (6%) H →L+1 (6%)
DMSO	283	4.382	258.73	4.793	38,650	0.4620	H ® L (85%) H-3 ® L (5%) H →L+1 (5%)
DMF			258.83	4.791	38,635	0.4660	H ® L (86%) H-3 ® L (5%) H →L+1 (5%)
2,2,2-Trifluoroethanol			257.94	4.807	38,769	0.4187	H ® L (82%) H-3 ® L (6%) H →L+1 (7%)
Benzonitrile			259.44	4.780	38,545	0.4941	H ® L (87%) H-3 ® L (4%) H →L+1 (5%)
Ethanol			258.43	4.798	38,695	0.4439	H ® L (84%) H-3 ® L (5%) H →L+1 (6%)
Benzyl alcohol			259.60	4.777	38,521	0.4965	H ® L (87%) H-3 ® L (4%) H →L+1 (5%)

[a][H–HOMO; L-LUMO]

Table 4
Solvent parameters and spectral properties of Fmoc-L-Glu(OtBu) compound.

Solvent	λ_{max} (nm)	υ^{-}(cm^{-1})	E_T (kcal/mol)	ε	n	Kamlet-Abboud-Tafta[a]		
						π^*	α	β
Chloroform	259.34	38,558.95	110.24	4.81	1.43	0.58	0.44	0.00
Methanol	258.19	38,731.55	110.74	33.70	1.33	0.59	0.93	0.66
water	258.17	38,734.78	110.75	78.30	1.33	1.09	1.02	0.18
DMSO	258.73	38,650.09	110.50	47.24	1.48	1.00	0.00	0.75
DMF	258.83	38,634.76	110.46	37.22	1.43	0.88	0.00	0.69
2,2,2-Trifluoroethanol	257.94	38,768.65	110.84	8.55	1.28	0.73	1.51	0.00
Benzonitrile	259.44	38,545.24	110.20	26.00	1.53	0.90	0.22	0.00
Ethanol	258.43	38,695.20	110.63	24.55	1.36	0.54	0.83	0.77
Benzyl alcohol	259.60	38,521.04	110.14	13.00	1.54	0.98	0.00	0.50

[a] Values taken from Ref. [60,61].

late the chemical's maximum absorptions λ_{max} (in nm) into molar transition energies $(E)_T$ in various solutions (Chloroform, Methanol, water, DMSO, DMF, 2,2,2-Trifluoroethanol, Benzonitrile, Ethanol, & Benzyl alcohol), and the results are listed in Table 4.

$$E_T = \frac{28591}{\lambda_{max}} (kacl/mol) \quad (3)$$

This molar transition energy (E_T) values indicate the stabilization of a chemical in a ground state for certain solutions**.** Table 4 provides the values in various solvents and this can be seen that the E_T value in water is the highest if compared to other solutions, showing that the probe molecules are strongly coupled to this solution, as well as the polar nature of the **Fmoc-L-Glu(OtBu)** in the ground state. The influence of various polar solvent and non-polar solvent interactions on solute stabilization was investigated using a multiparameter solvent polarity scale. The Kamlet–Abboud–Taft multilinear analysis, which is expressed in the following equation form, was first used in this regard **[**60,61**].**

$$\bar{\upsilon} = \bar{\upsilon} + \alpha\alpha + b\beta + c\pi* \quad (4)$$

Where $\bar{\upsilon}$ is the parameter of the solvatochromic interest (energy of absorptions in cm^{-1}); π^* α, & β are the ability of the hydrogen-bond donation and accepting solvents, respectively, whereas π^* index of the (dipolarity/polarizability) polarity solvents, respectively. Similarly, a, b, and c are independent coefficients. Multivariate regression was used to fit the absorption energies to the preceding equation, giving the following expression with relatively excellent correlations (R^2= 0.83154) obtained,

$$\bar{\upsilon} = 38404(\pm73) + 180(\pm28)a + 136(\pm42)\beta + 114(\pm71)\pi* \quad (5)$$

The greater value of β in Eq. (5)**,** indicates that hydrogen-bond accepting solvents have the greatest influence on the transition energy. The huge value α of in the Kamlet–Taft equation indicates that hydrogen-bond donating solutions have the most major impact on transition energy.

4.9. Donor-acceptor interactions analysis: NBO analysis

In molecular chemistry, the NBO (Natural bond orbital) analysis is essential for understanding different kinds of interactions between donor group molecules and acceptor group molecules with their stabilization energies, natural Lewis structure, and p-character with occupancy [62–64] In this work, the NBO calculation on the **Fmoc-L-Glu(OtBu)** addressed energy of stabilization with kinds of donor-acceptor bond interactions that were given in Table S5. The NBO simulation on the **Fmoc-L-Glu(OtBu)** was examined in this research, as well as the stabilization energy with various types of donor-acceptor interactions, as presented in Table S5. Interactions are mainly attributed to lone pair of oxygen & nitrogen atoms (e.g. O2, O3, O4, O5, O6, & N7) with anti-bonding groups of CH_2, CH_3, and benzene rings, which initiate charge transfer between natural bonds in a molecule

Table 5
Molecular docking results of binding energy (in kcal mol-1), inhibition constant (in μm), electrostatic energy (in kcal mol-1) intermolecular energy (in kcal mol-1), and ref. RMSD values (in Å) for the compound Fmoc-L-Glu(OtBu) with three different proteins (PDB code: 3PP0, 7EFJ, & 1OQA).

Protein (PDB code)	Type of organism	Ligand molecule	Binding affinity (kcal mol^{-1})	Inhibition constant (μm)	Electrostatic Energy (kcal mol^{-1})	Inter molecular energy (kcal mol^{-1})	Reference RMSD (Å)
3PP0	Homo sapiens	Fmoc-L-Glu(OtBu)	−4.19	855.42	−1.99	−7.47	50.74
7EFJ	Homo sapiens	Fmoc-L-Glu(OtBu)	−6.80	10.41	−1.44	−10.08	77.59
1OQA	Homo sapiens	Fmoc-L-Glu(OtBu)	−4.95	233.45	−1.00	−8.24	17.50

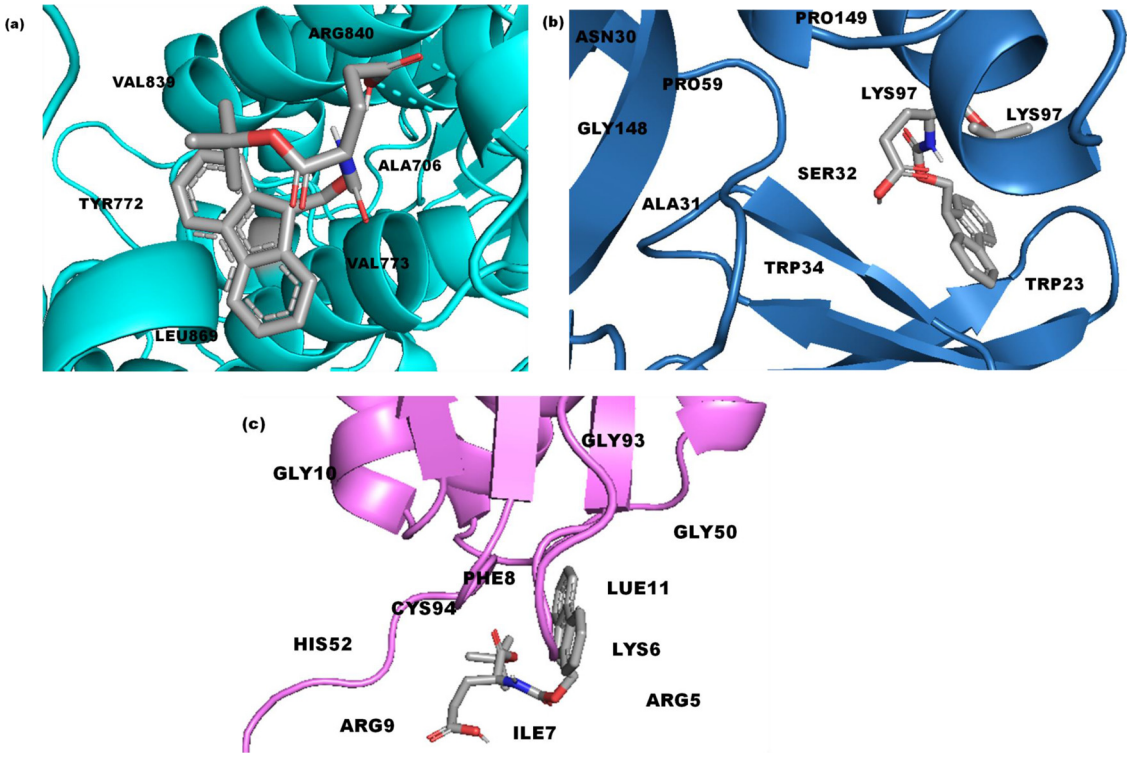

Fig. 10. The protein-ligand interactions with the best-docked pose of **Fmoc-L-Glu(OtBu)** with targeted proteins (a) 3PP0 (b) 7EFJ (c) 1OQA.

as well as increase their stability. The greatest interaction energy contributions of 3132, 1653, & 1032 kJ/mol were found for the transitions of LP(n)O3→σ^*(C28-H51), LP(n)O4→σ^*(C27-C31), & LP(n)O5→σ^*(C27-C31). Other types of interactions, such as π-π^*, σ-σ^*, σ-π^*, and π-σ^* were also identified and their stabilization energies were found in this case.

4.10. NLO properties: first-order hyperpolarizability prediction

Non-Linear Optical (NLO) properties are a method of evaluating the material's induced changes in optical strength, which are concerned with the examination of the relationship between high-intensity light and materials [65], and they were the most searched recent study due to their importance in interacting with significant activities. The dipole moment (μ), first-order Hyperpolarizability (β), and Plorizability (α) have been computationally determined in this study and are listed in Table S6. The computed values of dipole moments (μ) 1.884 Debye (Urea u = 0.9884D) and this higher value indicates that there are stronger substantial intermolecular interactions.; The first order hyperpolarizability of (β) the computed value of the **Fmoc-L-Glu(OtBu)** of 2113.68 × 10^{-33} e.s.u in comparison to urea [66], as a typical material (372.89 × 10^{-33} e.s.u) and which is 5.66 times higher than Urea.

4.11. Biological evaluations: molecular docking analysis

Molecular docking is an effective and suitable study for evaluating the compound's biological properties with target proteins and biomolecules. Using the PASS online tool [67], the highest possibility of action to Pin1 inhibitor was predicted. Pin1 is a unique enzyme responsible for the regulation that is usually found in tumor and normal cell molecules, where that colocalizes with many nucleoproteins. Pin1 is also involved in the development of cancer through canonical processes that take place in both the cytoplasmic and the nucleus [68]. Hence we selected three Pin1-specific proteins in tumor cells that are linked to human tumor cells for this study, such as (a) Kinase domain of Human HER2: erbB2 (PDB code: 3PP0) (b) Human Pin1 (PDB code: 7EFJ) and (c) BRCT-c domain from human BRCA1 (PDB code:1OQA) [69–71]. Table 5 and Fig. 10 show Protein-Ligand interactions with the best binding pose and Fig. S4, provides the H-bond donor-acceptor surfaces, binding parameters of binding affinity, inhibit activity rate, and so on. The non-bonded weak interaction forces are listed in Table 6 and visualized in Fig. 11. According to these results, the ligand of the title compound interacts with all target proteins of 3PP0, 7EFJ, & 1OQA. The compound **Fmoc-L-Glu(OtBu)** exhibited the highest energy of binding (−6.80 kcal/mol) with a larger weak contacts formation against the pin1 protein of cancer cell (Human Pin1 PDB

Table 6
The Non-covalent weak interactions between the Ligand Fmoc-L-Glu(OtBu) and three different proteins 3PP0,7EFJ, & 1OQA [*COHB - Conventional Hydrogen bond; PDHB -phi donor hydrogen bond; CAHB-Carbonyl Hydrogen Bond; UFAA - Unfavourable Acceptor-Acceptor; AKL-Alkyl; PAL- Phi-Alkyl; PPS - Phi-Phi Stack; PPTS- Phi T shaped; APS- Amide phi stacked; BEN - Benzene ring].

Ligand	Protein	Binding Energy (kcal mol^{-1})	Ligand group	Protein Residues	* Type of interaction	Distance (Å)
Fmoc-L-Glu(OtBu)	3PP0	−4.19	C=O	ALA706	COHB	3.57
			CO	ARG840	AKL	5.11
			BEN	VAL839	PAL	4.77
			BEN	VAL773	PAL	5.27
			BEN	TYR772	PPTS	5.38
			BEN	LEU869	PAL	6.97
Fmoc-L-Glu(OtBu)	7EFJ	−6.80	C=O	LYS97	COHB	4.82
			CO	SER32	COHB	4.30
			CO	LYS97	COHB	5.78
			BEN	TRP34	PPTS	4.14
			BEN	TRP23	PPS	5.26
			BEN	TRP34	PPS	5.05
Fmoc-L-Glu(OtBu)	1OQA	−5.00	OH	ARG9	COHB	3.96
			C=O	ILE7	CAHB	4.72
			BEN	PHE8	PLP	6.62
			BEN	CYS94	PSU	7.32
			BEN	CYS94	AKL	5.00

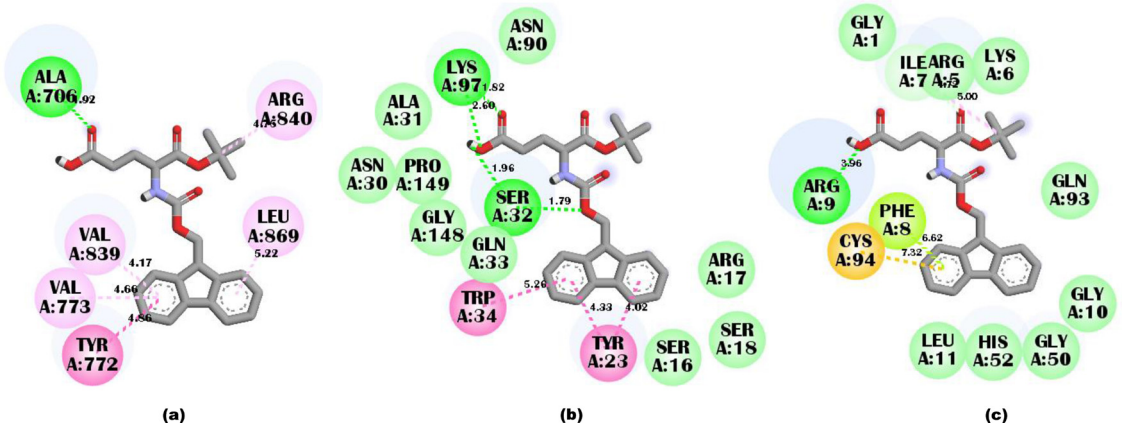

Fig. 11. The Non-covalent weak interactions between Fmoc-L-Glu(OtBu) and targeted proteins (a) 3PP0 (b) 7EFJ (c) 1OQA.

code: 7EFJ), from these findings three conventional Hydrogen bond connections are identified at carboxylic and carbonyl (C=O, CO) groups of title chemical and residue LYS97, SER32, & LYS97of protein with distances 4.82, 4.30, & 5.78 Å, respectively; one Phi T shaped interaction at TRP34 and benzene ring of the ligand with distance 4.14 Å; and two Phi-Phi Stack interactions were also found at TRP23 & TRP34 with distances 5.26 & 5.05 Å between ligand and protein.

5. Conclusion

In this work, The molecular structure of **Fmoc-L-Glu(OtBu)** was studied using FTIR and FT-Raman spectral techniques, as well as theoretical calculations using the B3LYP method. The previously reported results of strong self-assembled forces between chemical functionalities (C=O, COOH, NH, and OH) of the compound were confirmed by AIM, RDG, ELF, and LOL investigations of the **Fmoc-L-Glu(OtBu).** As a result of this process, the compound was more stable in the solvent phases, with more non-bonded interactions than in the gaseous form. Also, ELF and LOL studies concluded that the highest possible delocalization sites with chemical environments at C16-C21-C19 & C10-C15-C20 for gas-phase; C8-C13-O1 for Et_2O; and C30-C23-C29 for water, DMSO, & DMF. Due to the transition of the compound's LP(n)O3→σ^*(C28-H51), the maximum stabilization energy contribution was found in the NBO analysis. The calculated first-order hyperpolarizability of (β = 2084.984 $X10^{-33}$e.s.u) the value showed the good NLO property **of Fmoc-L-Glu(OtBu).** Against the Pin1 cancer cell (PDB: 7EFJ) development protein, which has the highest binding energy of −6.80 kcal/mol, the title chemical has the largest interaction energy and creates the more weak bonds.

Declaration of Competing Interest

None.

CRediT authorship contribution statement

M. Thirunavukkarasu: Conceptualization, Methodology, Validation, Formal analysis, Writing – original draft, Writing – review & editing, Visualization. **G. Balaji:** Investigation, Supervision, Project administration, Writing – original draft. **P. Prabakaran:** Methodology, Validation, Resources. **Shaik Jaheer Basha:** Methodology, Validation, Resources. **Ahmad Irfan:** Software, Methodology, Resources. **S Saleem Javed:** Validation, Methodology, Resources, Project administration. **S. Muthu:** Conceptualization, Software, Resources, Investigation, Supervision, Project administration, Writing – original draft.

Data availability

No data was used for the research described in the article.

Acknowledgment

A.Irfan extends his appreciation to the Deanship of Scientific Research at King Khalid University (KKU), Saudi Arabia for funding through research groups program under grant number R.G.P.2/30/43

Supplementary materials

Supplementary material associated with this article can be found, in the online version, at doi:10.1016/j.molstruc.2022.133793.

References

[1] L.A. Carpino, D. Sadat-Aalaee, H.G. Chao, [(9-Fluorenylmethyl)oxy]carbonyl (FMOC) amino acid fluorides. Convienient new peptide coupling reagents applicable to the FMOC/tert-butyl strategy for solution and solid-phase syntheses, J. Am. Chem. Soc. 112 (26) (1990) 9651–9652, doi:10.1021/ja00182a041.
[2] H. Schieb, S. Weidlich, G. Schlechtingen, Structural Design, Solid-Phase Synthesis and Activity of Membrane-Anchored β-Secretase Inhibitors on Aβ Generation from Wild-Type and Swedish-Mutant APP, Chem. Eur. J. 16 (2010) 14412–14423, doi:10.1002/chem.201002878.
[3] R. Merkx, K.E. Burns, P. Slobbe, F. El Oualid, et al., Synthesis and Evaluation of a Selective Fluorogenic Pup Derived Assay Reagent for Dop, a Potential Drug Target in *Mycobacterium tuberculosis*, ChemBioChem 13 (2012) 2056–2060, doi:10.1002/cbic.201200460.
[4] T.A. Kristedja, S.E. Park, R.K. Tiwari, Synthesis and Antiproliferative Activity of Hybrid Peptides for Ovarian and Prostate Cancer, Int. J. Pept. Res. Ther. 25 (2019) 1041–1048, doi:10.1007/s10989-018-9751-4.
[5] T. Assad, R. Mansour, I. Abou Hajar, Radiation chemistry, in: Synthesis of Hynic-TOC Peptide and Label it with ^{9}9mTc to be used in Tumor Diagnosis, and Synthesis and characterize of amino acids: Fmoc-Asp(OtBu)- OL, Fmoc-Glu(OtBu)- OL and Fmoc-Thr(tBu)- OL, 50, Syrian Arab Republic, 2017, pp. 1–65. https://inis.iaea.org/search/search.aspx?orig_q=RN:50071212.
[6] I. Truebenbach, J. Gorges, J. Kuhn, S. Kern, et al., Sequence-Defined Oligoamide Drug Conjugates of Pretubulysin and Methotrexate for Folate Receptor Targeted Cancer Therapy, Macromol. Biosci. 17 (2017) 1600520, doi:10.1002/mabi.201600520.
[7] B. Steinborn, I. Truebenbach, S. Morys, et al., Epidermal growth factor receptor targeted methotrexate and small interfering RNA co-delivery, J. Gene Med. 20 (2018) 7–8 e3041, doi:10.1002/jgm.3041.
[8] D.J. Lee, E. Kessel, D. Edinger, D. He, P.M. Klein, et al., Dual antitumoral potency of EG5 siRNA nanoplexes armed with cytotoxic bifunctional glutamyl-methotrexate targeting ligand, Biomaterials 77 (2016) 98–110, doi:10.1016/j.biomaterials.2015.11.004.
[9] X. Yao, Z. Zha, K. Ploessl, S.R. Choi, R. Zhao, et al., Synthesis and evaluation of novel radioiodinated PSMA targeting ligands for potential radiotherapy of prostate cancer, Bioorg. Med. Chem. 28 (2020) 115319, doi:10.1016/j.bmc.2020.115319.
[10] I. Güell, S. Vilà, L. Micaló, E. Badosa, et al., Eur. J. Org. Chem. 2013 (2013) 4933–4943, doi:10.1002/ejoc.201300215.
[11] Y.C. Hsiao, C.Y. Lee, Y.J. Lin, S.H. Tsai, K.C.G. Jeng, et al., Design, synthesis, and evaluation of fluorescent cell-penetrating peptidic antagonists of Grb2-SH2 for targeting MCF-7 breast cancer cells, Med. Chem. Res. 22 (2013) 5337–5343, doi:10.1007/s00044-013-0538-z.
[12] D. Cardella, L.Y.P. Luk, Y.H. Tsai, Conjugation of proapoptotic peptides with folate and cyanine dyes for enhanced potency and selectivity towards tumor cell lines, chemrxiv.org, v1 (2021), 1-20, doi:10.26434/chemrxiv-2021-qn8wb.
[13] P. Coghi, J.P.L. Ng, O. Kadioglu, B.Y.K. Law, A.C. Qiu, et al., Synthesis, computational docking and biological evaluation of celastrol derivatives as dual inhibitors of SERCA and P-glycoprotein in cancer therapy, Eur. J. Med. Chem. 224 (2021) 113676, doi:10.1016/j.ejmech.2021.113676.
[14] C.H. Chen, M.K. Chen, K.C.G. Jeng, et al., Effects of Peptidic Antagonists of Grb2-SH2 on Human Breast Cancer Cells, Protein Pept. Lett. 17 (2010) 44–53, doi:10.2174/092986610789909421.
[15] L. Shan, M. Liu, C. Wu, L. Zhao, S. Li, L. Xu, et al., Multi-small molecule conjugations as new targeted delivery carriers for tumor therapy, Int. J. Nanomed. 10 (2015) 5571–5591, doi:10.2147/IJN.S85402.
[16] K. Hu, X. Tang, G. Tang, S. Yao, B. Yao, H. Wang, D. Nie, et al., .sup.18F-FP-PEG.sub.2-[beta]-Glu-RGD.sub.2: A Symmetric Integrin [alpha].sub.v[beta].sub.3-Targeting Radiotracer for Tumor PET Imaging, Plos ONE (2015) 1–13, doi:10.1371/journal.pone.0138675.
[17] D.M. Ryan, S.B. Anderson, B.L. Nilsson, The influence of side-chain halogenation on the self-assembly and hydrogelation of Fmoc-phenylalanine derivatives, Soft Matter 6 (2010) 3220–3231, doi:10.1039/C0SM00018C.
[18] C. Tang, R.V. Ulijn, A. Saiani, Effect of Glycine Substitution on Fmoc–Diphenylalanine Self-Assembly and Gelation Properties, Langmuir 27 (2011) 14438–14449, doi:10.1021/la202113j.
[19] D.A. Wellings, E. Atherton, Standard Fmoc protocols, Methods Enzymol. 28 (1997) 44–67, doi:10.1016/S0076-6879(97)89043-X.
[20] K. Yamada, D. Hashizume, T. Shimizu, et al., A solid-state ^{17}O NMR, X-ray, and quantum chemical study of N-α-Fmoc-protected amino acids, J. Mol. Struct. 888 (2008) 187–196, doi:10.1016/j.molstruc.2007.11.059.
[21] K. Yamada, D. Hashizume, T. Shimizu, N-(fluoren-9-ylmethoxycarbonyl)-laspartic acid 4-tert-butyl ester, Acta Crystallogr. E65 (2009) o2606–o2607, doi:10.1107/S1600536809037611.
[22] K. Yamada, D. Hashizume, T. Shimizu, N-(fluoren-9-ylmethoxycarbonyl)-L isoleucine, Acta Crystallogr. E64 (2008) o1533, doi:10.1107/S1600536808021855.
[23] J. Bojarska, M. Remko, I.D. Madura, et al., Synthesis, experimental and *in silico* studies of *N*-fluorenyl-methoxycarbonyl-*O*-*tert*-butyl-*N*-methyl-tyrosine, coupled with CSD data: a survey of inter-actions in the crystal structures of Fmoc–amino acids, Acta Crystallogr. C76 (2020) 328–345, doi:10.1107/S2053229620003009.
[24] K. Yamada, D. Hashizume, T. Shimizu, K. Deguchi, N-(Fluoren-9-ylmethoxycarbonyl)-L leucine, Acta Crystallogr. E64 (2008) o1112, doi:10.1107/S1600536808014372.
[25] W. Clegg, L. Horsburgh, Methyl 2(S)-(N-fluoren-9-ylmethoxy-carbonylamino)-3-(2-pyridyl)propionate, Acta Crystallogr. E59 (2003) o1257–o1258, doi:10.1107/S1600536803017240.
[26] W. Clegg, L. Horsburgh, tert-Butyl (2R)-2-(9H-Fluoren-9-ylmethoxy-carbonylamino)-3-iodopropionate, Acta Crystallogr. E59 (2003) o1925–o1926, doi:10.1107/S1600536803025467.
[27] M.J. Frisch, G.W. Trucks, H.B. Schlegel, G.E. Scuseria, M.A. Robb, J.R. Cheeseman, G. Scalmani, V. Barone, B. Mennucci, G.A. Petersson, H. Nakatsuji, M. Caricato, X. Li, H.P. Hratchian, A.F. Izmaylov, J. Bloino, G. Zheng, J.L. Sonnenberg, M. Hada, M. Ehara, K. Toyota, R. Fukuda, J. Hasegawa, M. Ishida, T. Nakajima, Y. Honda, O. Kitao, H. Nakai, T. Vreven, J.A. Montgomery, Jr., J.E. Peralta, F. Ogliaro, M. Bearpark, J.J. Heyd, E. Brothers, K.N. Kudin, V.N. Staroverov, R. Kobayashi, J. Normand, K. Raghavachari, A. Rendell, J.C. Burant, S.S. Iyengar, J. Tomasi, M. Cossi, N. Rega, J.M. Millam, M. Klene, J.E. Knox, J.B. Cross, V. Bakken, C. Adamo, J. Jaramillo, R. Gomperts, R.E. Stratmann, O. Yazyev, A.J. Austin, R. Cammi, C. Pomelli, J.W. Ochterski, R.L. Martin, K. Morokuma, V.G. Zakrzewski, G.A. Voth, P. Salvador, J.J. Dannenberg, S. Dapprich, A.D. Daniels, O. Farkas, J.B. Foresman, J.V. Ortiz, J. Cioslowski, D.J. Fox, Gaussian, Inc., Wallingford CT, Gaussian 09, Revision A.02, 2009.
[28] T. Lu, F. Chen, Multiwfn: A multifunctional wavefunction analyzer, J. Comput. Chem. 33 (2012) 580–592, doi:10.1002/jcc.22885.
[29] AIMAll (Version 19.10.12), Todd A. Keith, T.K Gristmill Software, Overland Park KS, USA, 2019 (aim.tkgristmill.com), URL: http://aim.tkgristmill.com/readme.html
[30] M. Karabacak, E. Kose, E.B. Sas, M. Kurt, A.M. Asiri, A. Atac, DFT calculations and experimental FT-IR, FT-Raman, NMR, UV–Vis spectral studies of 3-fluorophenylboronic acid, Spectrochim. Acta Part A 136 (2015) 306–320, doi:10.1016/j.saa.2014.08.141.
[31] M.H. Jamroz, Vibrational energy distribution analysis VEDA 4, Warsaw, 2004-2010, https://smmg.pl/software
[32] J.P. Perdew, M. Levy, Physical content of the exact kohn-sham orbital energies: band gaps and derivative discontinuities, Phys. Rev. Lett. 51 (20) (1983) 1884–1887, doi:10.1103/PhysRevLett.51.1884.
[33] R.G. Parr, R.G. Pearson, Absolute hardness: companion parameter to absolute electronegativity, J. Am. Chem. Soc. 105 (1983) 7512–7516, doi:10.1021/ja00364a005.
[34] J.P. Perdew, R.G. Parr, M. Levy, J.L. Balduz, Density-functional theory for fractional particle number: derivative discontinuities of the energy, Phys. Rev. Lett. 49 (23) (1982) 1691–1694, doi:10.1103/PhysRevLett.49.1691.
[35] J.F. Janak, Proof that $\partial E/\partial ni=\varepsilon$in density-functional theory, Phys. Rev. B. 18 (12) (1978) 7165–7168, doi:10.1103/PhysRevB.18.7165.
[36] R.G. Pearson, "Absolute electronegativity and hardness correlated with molecular orbital theory", Proc. Natl. Acad. Sci. U. S. A. 83 (1986) 8440–8441, 10.1073/pnas.83.22.8440
[37] R.G. Parr, L.V. Szentpaly, S. Liu, Electrophilicity Index, J. Am. Chem. Soc. 121 (1999) 1922–1924, doi:10.1021/ja983494x.
[38] M.E. Casida, C. Jamorski, K.C. Casida, et al., Molecular excitation energies to high-lying bound states from time-dependent density-functional response theory: characterization and correction of the time-dependent local density approximation ionization threshold, J. Chem. Phys. 108 (1998) 4439–4449, doi:10.1063/1.475855.
[39] G. Scalmani, M.J. Frisch, B. Mennucci, Geometries and properties of excited states in the gas phase and in solution: theory and application of a time-dependent density functional theory polarizable continuum model, J. Chem. Phys. 124 (9) (2006) 1–15 094107, doi:10.1063/1.2173258.
[40] G.M. Morris, R. Huey, W. Lindstrom, AutoDock4 and AutoDockTools4: Automated docking with selective receptor flexibility, J. Comput. Chem. 30 (2009) 2785–2791, doi:10.1002/jcc.21256.
[41] N.A Wani, V.K. Gupta, R. Kant, S. Aravinda, R. Rai, et al., Conformation and crystal structures of 1-amino-cyclo-hexa-neacetic acid ($\beta^{3,3}$Ac$_6$c) in N-protected derivatives, Acta. Crystallogr. Sect. E. Struct. Rep. Online. E70 (2014) 272–277, doi:10.1107/S1600536814020777.
[42] K. Sangeetha, S.R. Rajina, M.K. Marchewka, J. Binoy, The study of inter and intramolecular hydrogen bonds of NLO crystal melaminium hydrogen malonate using DFT simulation, AIM analysis and Hirshfeld surface analysis, Mater. Today Proc. 25 (2020) 307–315, doi:10.1016/j.matpr.2020.01.526.
[43] P. Srinivasan, S.N. Asthana, RB. Pawar, P. Kumaradhas, A theoretical charge density study on nitrogen-rich 4,4′,5,5′-tetranitro-2,2′-bi-1H-imidazole (TNBI) energetic molecule, Struct. Chem. 22 (2011) 1213–1220, doi:10.1007/s11224-011-9815-y.
[44] M. Thirunavukkarasu, G. Balaji, S. Muthu, et al., Theoretical conformations studies on 2-Acetyl-gamma-butyrolactone structure and stability in aqueous

phase and the solvation effects on electronic properties by quantum computational methods, Comput. Theor. Chem. 1208 (2022) 113534, doi:10.1016/j.comptc.2021.113534.
[45] S. Al-Otaibi, Y.S. Mary, Y.S. Mary, et al., Conformational, Reactivity Analysis, Wavefunction-Based Properties, Molecular Docking and Simulations of a Benzamide Derivative with Potential Antitumor Activity-DFT and MD Simulations, Polycycl. Aromat. Compd. (2022) 1–18, doi:10.1080/10406638.2022.2039229.
[46] G. Golding Sheeba, D. Usha, M. Amalanathan, M. Sony Michael Mary, Identification of structure activity relation of a synthetic drug 2, 6-pyridine dicarbonitrile using experimental and theoretical investigation, Wutan Huatan Jisuan Jishu XVI (2020) 89–113 UL http://wthtjsjs.cn/gallery/11-whjj-nov-5684.pdf .
[47] C.S. Abraham, S. Muthu, J.C. Prasana, B.F. Rizwana, Vibrational and electronic absorption spectroscopic profiling, natural hybrid orbital, charge transfer, electron localization function and molecular docking analysis on 3-amino-3-(2-nitrophenyl) propionic acid, J. Mol. Struct. 1171 (2018) 733–746, doi:10.1016/j.molstruc.2018.06.057.
[48] A. Raj, K. Raju, H.T. Varghese, CM. Granadeiro, HI.S. Nogueirad, C. Yohannan Panicker, IR, Raman and SERS spectra of 2-(methoxycarbonylmethylsulfanyl)-3,5-dinitrobenzene carboxylic acid, J. Braz. Chem. Soc. 20 (3) (2009) 549–559 URLhttps://www.scielo.br/j/jbchs/a/wH86MZ6MMW5vsRc3nPwCVhx/?format=pdf&lang=en.
[49] S. Chandra, H. Saleem, S. Sebastian, N. Sundaraganesan, The spectroscopic (FT-IR, FT-Raman), NCA, first order hyperpolarizability, NBO analysis, HOMO and LUMO analysis of l-cysteine by ab inito HF and density functional method, Spectrochim. Acta Part A 78 (2011) 1515–1524, doi:10.1016/j.saa.2011.01.043.
[50] T. Rajamani, S. Muthu, M. Karabacak, Electronic absorption, vibrational spectra, nonlinear optical properties, NBO analysis and thermodynamic properties of N-(4-nitro-2-phenoxyphenyl) methanesulfonamide molecule by ab initio HF and density functional methods, Spectrochim. Acta Part A 108 (2013) 186–196, doi:10.1016/j.saa.2013.01.090.
[51] S. Muthu, E.E. Porchelvi, M. Karabacak, A.M. Asiri, Synthesis, structure, spectroscopic studies (FT-IR, FT-Raman and UV), normal coordinate, NBO and NLO analysis of salicylaldehyde p-chlorophenylthiosemicarbazone, J. Mol. Struct. 1081 (2015) 400–412, doi:10.1016/j.molstruc.2014.10.024.
[52] M. Pandey, S. Muthu, N.M.N. Gowda, Quantum mechanical and spectroscopic (FT-IR, FT-Raman,^{1}H,^{13}C NMR, UV-Vis) studies, NBO, NLO, HOMO, LUMO and Fukui function analysis of 5-Methoxy-1H-benzo[d]imidazole-2(3H)-thione by DFT studies, J. Mol. Struct. 1130 (2017) 511, doi:10.1016/j.molstruc.2016.10.064.
[53] S. Muthu, A. Prabhakaran, Vibrational spectroscopic study and NBO analysis on tranexamic acid using DFT method, Spectrochim. Acta Part A 129 (2014) 184–192, doi:10.1016/j.saa.2014.03.050.
[54] M. Karabacak, Z. Cinar, M. Kurt, S. Sudha, N. Sundaraganesan, FT-IR, FT-Raman, NMR and UV–vis spectra, vibrational assignments and DFT calculations of 4-butyl benzoic acid, Spectrochim. Acta Part A 85 (2012) 179–189, doi:10.1016/j.saa.2011.09.058.
[55] C.S. Abraham, J.C. Prasana, S. Muthu, M. Raja, Quantum computational studies, spectroscopic (FT-IR, FT-Raman and UV–Vis) profiling, natural hybrid orbital and molecular docking analysis on 2,4 Dibromoaniline, J. Mol. Struct. 1160 (2018) 393–405, doi:10.1016/j.molstruc.2018.02.022.
[56] S. Gunasekaran, S. Seshadri, S. Muthu, S. Kumaresan, R. Arunbalaji, Vibrational spectroscopy investigation using ab initio and density functional theory on p-anisaldehyde, Spectrochim. Acta Part A 70 (2008) 550–556, doi:10.1016/j.saa.2007.07.050.
[57] J.S. Murray, P. Politzer, The electrostatic potential: an overview, Wiley Interdiscip. Rev. Comput. Mol. Sci. 1 (2011) 153–163, doi:10.1002/wcms.19.
[58] M. Thirunavukkarasu, G. Balaji, S. Muthu, et al., Computational spectroscopic investigations on structural validation with IR and Raman experimental evidence, projection of ultraviolet-visible excitations, natural bond orbital interpretations, and molecular docking studies under the biological investigation on N-Benzyloxycarbonyl-L-Aspartic acid 1-Benzyl ester, Chem. Data Collect. 31 (2021) 100622, doi:10.1016/j.cdc.2020.100622.
[59] C. Adamo, D. Jacquemin, The calculations of excited-state properties with time-dependent density functional theory, Chem. Soc. Rev. 42 (2013) 845–856, doi:10.1039/C2CS35394F.
[60] M.J. Kamlet, J.L. Abboud, R.W. Taft, The solvatochromic comparison method. 6. The .pi.* scale of solvent polarities, J. Am. Chem. Soc. 99 (1977) 6027–6038, doi:10.1021/ja00460a031.
[61] M.J. Kamlet, R.W. Taft, The solvatochromic comparison method. I. The .beta.-scale of solvent hydrogen-bond acceptor (HBA) basicities, J. Am. Chem. Soc. 98 (1976) 377–383, doi:10.1021/ja00418a009.
[62] J.P. Foster, F. Weinhold, Natural hybrid orbitals, J. Am. Chem. Soc. 102 (1980) 7211–7218, doi:10.1021/ja00544a007.
[63] A.E. Reed, R.B. Weinstock, F. Weinhold, Natural-population analysis, J. Chem. Phys. 83 (1985) 735–746, doi:10.1063/1.449486.
[64] A.E. Reed, F. Weinhold, Natural localized molecular orbitals, J. Chem. Phys. 83 (1985) 1736–1740, doi:10.1063/1.449360.
[65] T. Manickavelu, B. Govindrajan, M. Sambantham, Computational investigation, effects of polar and non-polar solvents on optimized structure with topological parameters (ELF, LOL, AIM, and RDG) of three glycine derivative compounds, Struct. Chem. (2022), doi:10.1007/s11224-022-01930-2.
[66] T.K. Kuruvilla, S. Muthu, J.C. Prasana, J. George, Spectroscopic (FT-IR, FT-Raman), quantum mechanical and docking studies on methyl[(3S)-3-(naphthalen-1-yloxy)-3-(thiophen-2-yl)propyl]amine, J. Mol. Struct. 1175 (2019) 163–174, doi:10.1016/j.molstruc.2018.07.097.
[67] A. Lagunin, A. Stepanchikova, D. Filimonov, V. Poroikov, PASS: prediction of activity spectra for biologically active substances, Bioinformatics 16 (2000) 747–748, doi:10.1093/bioinformatics/16.8.747.
[68] B.J. Pinch, Z.M. Doctor, B. Nabet, C.M. Browne, et al., Identification of a potent and selective covalent Pin1 inhibitor, Nat. Chem. Biol. 16 (2020) 979–987 volume, doi:10.1038/s41589-020-0550-9.
[69] L. Liu, R. Zhu, J. Li, Y. Pei, S. Wang, P. Xu, et al., Computational and Structure-Based Development of High Potent Cell-Active Covalent Inhibitor Targeting the Peptidyl-Prolyl Isomerase NIMA-Interacting-1 (Pin1), J. Med. Chem. 65 (2022) 2174–2190, doi:10.1021/acs.jmedchem.1c01686.
[70] K. Aertgeerts, R. Skene, J. Yano, B.C. Sang, H. Zou, et al., Structural Analysis of the Mechanism of Inhibition and Allosteric Activation of the Kinase Domain of HER2 Protein, J. Biol. Chem. 286 (2011) 18756–18765, doi:10.1074/jbc.M110.206193.
[71] O.J. Gaiser, L.J. Ball, P. Schmieder, D. Leitner, et al., Solution Structure, Backbone Dynamics, and Association Behavior of the C-Terminal BRCT Domain from the Breast Cancer-Associated Protein BRCA1, Biochemistry 43 (2004) 15984–15994, doi:10.1021/bi049550q.